Journal of Hydrology 598 (2021) 126441

Contents lists available at ScienceDirect

Journal of Hydrology

journal homepage: www.elsevier.com/locate/jhydrol

Research papers

Impacts of fluvial flood on physical and biogeochemical environments in estuary–shelf continuum in the East China Sea

Jianzhong Ge [a,b,*], Jingsi Zhang [a], Changsheng Chen [c], Pingxing Ding [a,b]

[a] State Key Laboratory of Estuarine and Coastal Research, East China Normal University, Shanghai, 200241, China
[b] Institute of Eco-Chongming (IEC), Chenjiazhen, Shanghai 202162, China
[c] School for Marine Science and Technology, University of Massachusetts-Dartmouth, New Bedford, MA 02744, United States

ARTICLE INFO

This manuscript was handled by Marco Borga, Editor-in-Chief

Keywords:
Fluvial flood
Three Gorges Dam
Changjiang River
East China Sea
Nutrients

ABSTRACT

Land-ocean interaction plays an essential role in the transport fate of terrestrial matters in the coastal and shelf regions. Flood discharge from a mega river, containing massive water, sediment, and nutrient loads, could result in substantial and complex impacts on the physical and biogeochemical dynamics of coastal systems. In this study, field campaigns were conducted in a region from the Changjiang River Estuary to the East China Sea (ECS) before and after a significant flood. The impacts of the flood on physical and biogeochemical environments were assessed. The results revealed that the fluvial flood enhanced the offshore expansion of the low-salinity river plume and associated sediment/nutrient fronts. However, the area of elevated chlorophyll-a at the river mouth did not expand noticeably. A numerical model was applied to quantify the contribution of the Three Gorges Dam (TGD) to the spatial intensity and temporal duration of fluvial flood effects on estuary–shelf continuum. The results predicted a maximum of 2° latitudinal offshore displacement of the shelf water. Salinity and nitrate exhibited conservative expansions, with a longer relaxation time (~2 months) than chlorophyll-a and phosphate. After the TGD-regulated flow event ceased, salinity and nitrate effects persisted, but phosphate and chlorophyll-a recovered rapidly. The flood decreased the dissolved oxygen (DO) concentration around the river mouth and the offshore region, but not in the nearshore transient area. In contrast, the non-TGD regulation increased the regional DO concentration, which reduced the hypoxia risk. The TGD has become a crucial anthropogenic driver of environmental changes in the Changjiang Estuary-ECS continuum.

1. Introduction

The estuary–shelf continuum, an area where terrestrial and oceanic waters meet, is a dynamic zone with energetic physical and biogeochemical interactions. This area is significantly influenced not only by seasonal variabilities caused by freshwater discharges, sediments from catchment soils, and dissolved or particulate organic/inorganic nutrients but also by irregular and extreme hydrological events, such as droughts and floods (Dittmann et al., 2015; O'Mara et al., 2019). Fluvial flood waves are a globally common dynamic feature in many estuaries connecting with river networks, such as the Elbe–German Bight (Voynova et al., 2017), the Changjiang Estuary (CE)–East China Sea (ECS) (Chen et al., 2017; Gong et al., 2011), the Po River–Adriatic Sea (Zoppini et al., 2019), and the Mississippi River (Gierach et al., 2013; Roy et al., 2013). During river floods, terrestrial matters, mixed with runoff, estuarine, and oceanic waters, are delivered to the estuary–shelf continuum, resulting in unusual changes in local or regional ecosystems and biogeochemistry environments (Wetz and Yoskowitz, 2013; Gopal et al., 2017). Since nonlinear physical and biogeochemical interaction processes drive these changes, it is difficult to identify and quantify flood-induced net physical and biogeochemical contributions due to limited observations.

Anthropogenic damming activities are common in most river systems and drainage basins, further influencing the estuarine physical and biogeochemical interaction processes (Milliman and Farnsworth, 2011; Yang et al., 2011, 2015). Dams regulate downstream runoff and sediments, increasing the complexity of physical and biogeochemical responses to river floods in the estuary–shelf continuums. It is a challenge to distinguish the relative influences of dam regulation and river flood waves on estuarine ecosystems solely through field observations, even if the amount of the water flowing through a dam is known. A model-based experiment in a flood context could be an effective method to determine

* Corresponding author at: State Key Laboratory of Estuarine and Coastal Research, East China Normal University, Shanghai 200241, China.
E-mail address: jzge@sklec.ecnu.edu.cn (J. Ge).

https://doi.org/10.1016/j.jhydrol.2021.126441
Received 28 July 2020; Received in revised form 4 May 2021; Accepted 5 May 2021
Available online 8 May 2021

the relative impacts of the fluvial flood and dam on these physical/biogeochemical processes (Kerimoglu et al., 2020).

The Three Gorges Dam (TGD), at the middle reach of the Changjiang River, China, is the world's largest hydroelectric dam (Huang et al., 2019). The water regulated by this dam has caused dramatic ecological changes in the CE–ECS continuum, not only in the frequency and timing of harmful phytoplankton blooms (Chen et al., 2003b; Gao et al., 2019; Zhang et al., 2016), but also in the spatiotemporal variability of salinity plumes, suspended sediment fronts, and nutrient concentrations (Feng et al., 2014). To verify the anthropogenic influence of the TGD regulation during river flood events on the estuarine water quality in the Changjiang River, two field survey cruises were conducted to sample

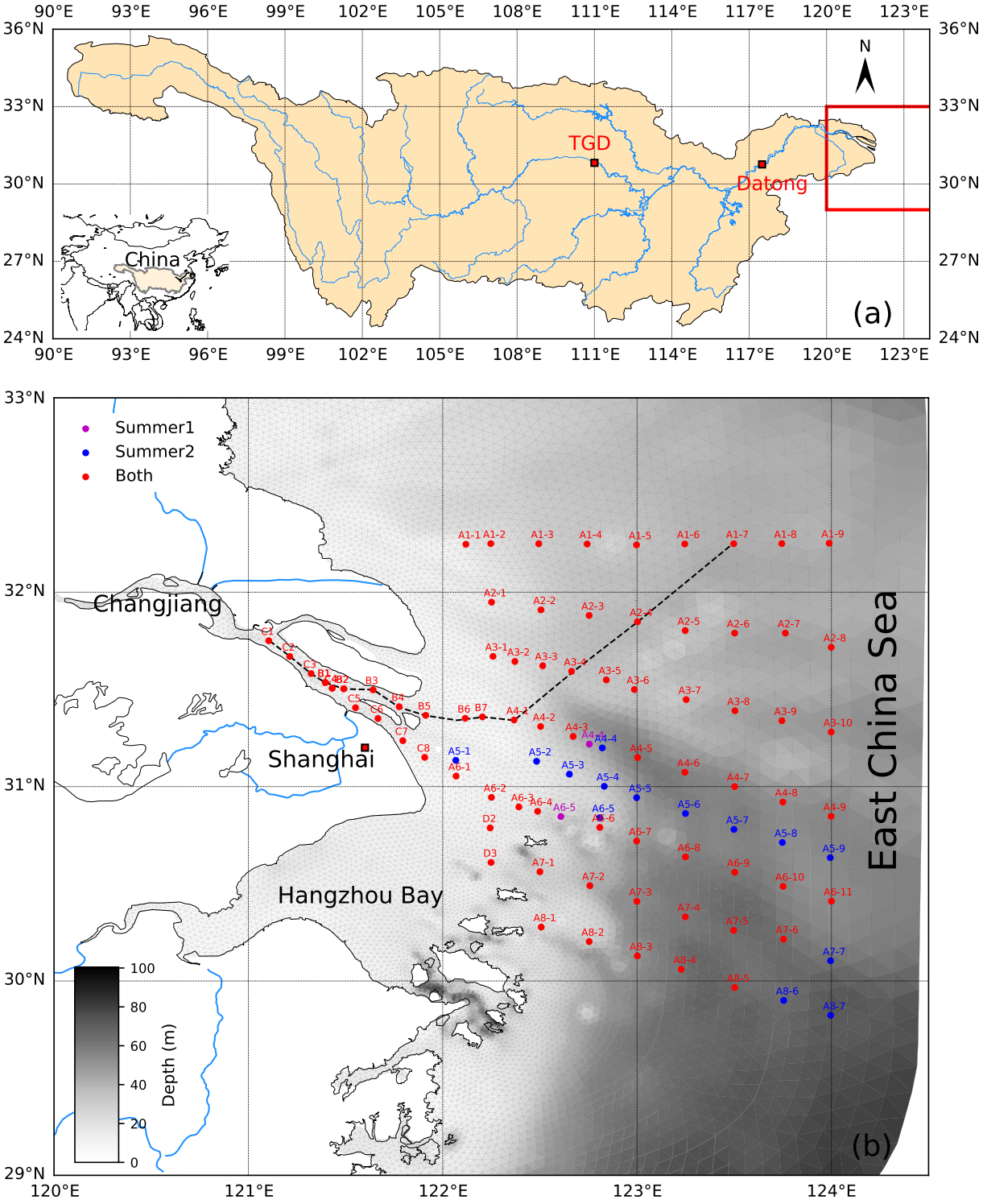

Fig. 1. Map of the study area. (a) Changjiang River drainage basin and Changjiang Estuary (red rectangle), Three Gorges Dam (TGD), and Datong hydrological station. (b) An enlarged view of the inner shelf of the East China Sea overlapped with survey sites of two field survey cruises. Magenta, blue, and red dots: measurement sites made for the first, second, and both surveys, respectively. The light gray lines in (b): the triangular model mesh. The dashed line: a selected transect from the river channel (C1) to the offshore region (A1-7) for analysis. (For interpretation of the references to color in this figure legend, the reader is referred to the web version of this article.)

physical and ecological variables from the estuary to the inner shelf of the ECS before and after a flood in July 2016. During this river flood, the runoff peak was approximately 7 × 10^4 m^3/s. The objectives of this study were to (1) estimate spatiotemporal variations in the local physical and biogeochemical environment under extreme flood conditions and (2) distinguish and quantify the relative contributions of river flood and water regulation of the TGD to these variations. To achieve these objectives, observed salinity, nutrient, and phytoplankton concentrations were first simulated using a validated physical-biogeochemical coupled model system. A series of process-oriented experiments were then conducted to quantify the relative impacts of the flood and TGD regulation on local and regional ecosystems.

2. Study area, observations, and model

2.1. Study area

The Changjiang River and its drainage basin were the flood source area, in which the flood directly influences freshwater runoff, sediment, dissolved/particulate inorganic/organic nutrients, and other pollutants (Fig. 1a). The Changjiang River originates from the Qinghai–Tibet Plateau and has a total length of about 6300 km. The Changjiang River is the third-longest river in the world and the most extensive river system in Asia. It has many tributaries, including the Jingsha, Yalong, Jiaming, Minjiang, Hanjiang, and Ganjiang Rivers in the upstream region. These tributaries join the lower reaches of the Changjiang River through Datong station, the nearest hydrological station to the CE. The CE–ECS continuum is a sink area of flood-induced loading (Fig. 1b). This continuum is a shallow continental shelf area with a depth varying from approximately 10 m in the river mouth to about 50 m in the inner shelf of the ECS (Fig. 1b). Hangzhou Bay is the southern bound of the CE–ECS continuum, which is a flow-through area of the offshore CE water and a CE sediment deposition region. The Changjiang River average runoff is 4 × 10^4 m^3/s during the wet season (Luan et al., 2016). During the 1998 and 2010 river flood periods, the runoff was up to 7.4 × 10^4 and 6.05 × 10^4 m^3/s, respectively (Gong et al., 2011), providing an additional 2–3 × 10^4 m^3/s freshwater into the CE–ECS continuum.

The TGD, the world's largest hydroelectric dam, is located at the middle reach of the Changjiang River (Fig. 1a). It has a total capacity of 39.3 km^3. At full capacity, the highest water level can reach 175 m (Jiao et al., 2007). This dam mainly regulates the runoff rate through the impoundment and discharge schemes during the wet and dry seasons. In addition to controlling the water flux for hydropower generation, water regulation can be adjusted to manage disastrous flooding that plagues the Changjiang drainage basin (Tullos, 2009). This method worked well to avoid a regionally wide catastrophic flooding in July 2010 and 2012 (Xinhua Net, 2010, 2012; Xu et al., 2013).

2.2. Surveys and data

The Changjiang Drainage basin was at a river flood warning level on July 1, 2016. On this date, the flood-induced water washed into the TGD at a rate of 5.0 × 10^4 m^3/s. Through regulation, the TGD released the water into the downstream estuarine region at a rate of 3.1 × 10^4 m^3/s. This rate was about 2.0 × 10^4 m^3/s more than usual, which helped reduce the water volume in the TGD reservoir in the upstream regions and prevented the Changjiang Drainage basin from flood risk (Zhang and Chen, 2017; Zheng, 2017). The Datong gauge station experienced a peak freshwater discharge at a rate of 7.0 × 10^4 m^3/s on July 12 (Fig. 2). The discharge value remained higher than 6.0 × 10^4 m^3/s until August 1, even though it gradually declined with time.

To examine the impacts of the river flood wave on the local ecosystem, two field surveys were conducted in the CE–ECS continuum in July 2016 (Fig. 1b). The measurements for these two surveys were made on similar transects from the CE to the inner shelf of the ECS. The first survey was carried out on July 4–15, including 75 stations. The second survey was conducted on July 19–28, including 87 stations. In this survey, in addition to repeating measurements at 75 stations of the first survey, additional 12 sampling sites were added; nine were in the center of the survey area (A5-1 to A5-9) and three in the southeastern region (Fig. 1b). The distance from the Datong station to the CE–ECS continuum was about 620 km. The river flood peak wave at Datong station occurred on July 12 and took 5–7 days to arrive at the river mouth. Therefore, the first and second surveys represented pre- and post-flood conditions in the CE–ECS continuum. At each site, the same physical and biogeochemical variables were measured at three levels

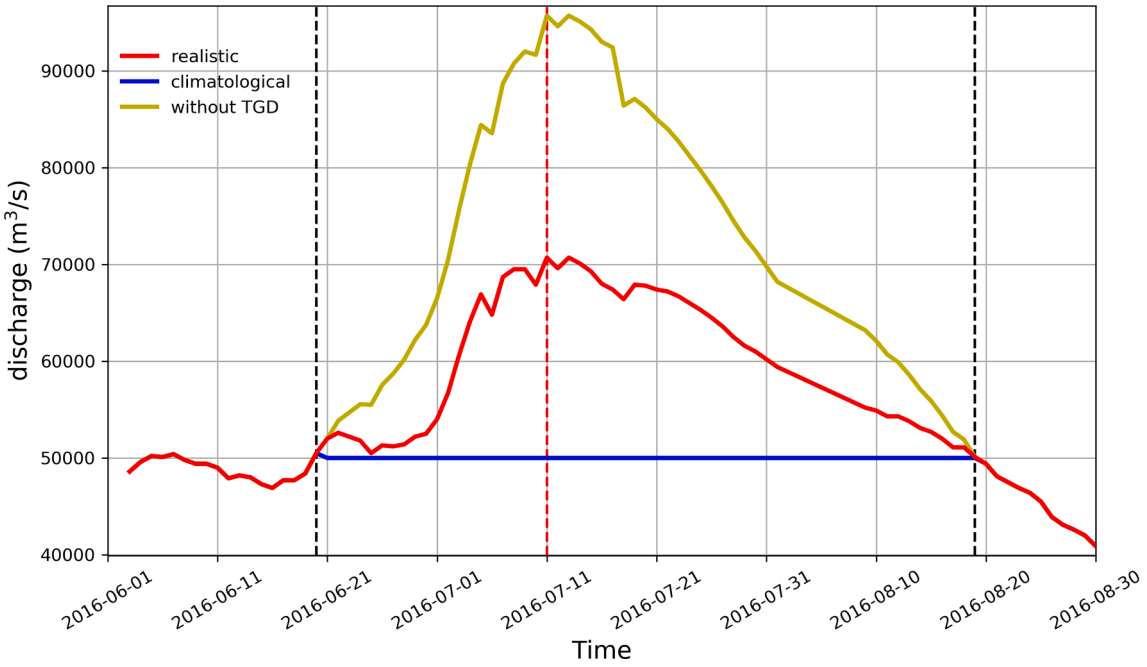

Fig. 2. River discharge rates at Datong hydrological station for the realistic (red), climatological (blue), non-TGD (yellow) cases. Three dashed lines indicate the time for June 20, July 11, and August 19, 2016. (For interpretation of the references to color in this figure legend, the reader is referred to the web version of this article.)

near the surface, middle depth, and the bottom. These variables included salinity, temperature, suspended particulate matter (SPM), dissolved inorganic nitrate, silicate, phosphate, dissolved oxygen (DO) and chlorophyll-a (*Chl a*) concentrations. The salinity and temperature were measured in-situ by the SBE 25-plus Sealogger CTD. SPM was determined by direct water samplings, then filtered and weighed in our laboratory. The collected water samples were also in-situ filtered right away with Whatman GF/F filters (pore size 0.7μ m), then sterilized with 1.5‰ (v/v) saturated $HgCl_2$ solution and stored at 4 °C. The slow thawing processes were applied to measure the concentration of dissolved inorganic nitrate, silicate, phosphate with an automatic nutrient analyzer equipment (QuAAtro, Seal Analytical, Germany) (Dore et al., 1996; Zhang and Ortner, 1998; Gao et al., 2015). The detection limits of nitrate, silicate, and phosphate were 0.14 μM, 0.07 μM, and 0.06 μM, respectively. The *Chl a* concentration was analyzed with a fluorometer (Trilogy, Turner Design, CA, USA). The dissolved oxygen concentration in seawater was measured by iodometry method. The DO concentration of <2.0 mg/L (62.5 mmol O_2 m^{-3}) is defined as hypoxia, following Fennel and Testa (2019).

2.3. Model system and configurations

Data collected from the two field surveys elucidated changes in the physical and biogeochemical environments of the CE–ECS continuum before and after the river flood. However, since the TGD released a large amount of water through regulation, it was difficult to distinguish the river flood impacts solely from the field measurement data. To maximize the spatial and time coverage, we arranged the field surveys over a two-week time scale. The weather and estuary/ocean conditions (tidal and subtidal currents) varied significantly during those periods. The tidal flow experienced a neap and spring tidal cycle over a fortnight period. The northward wind prevailed most of the time in July 2016, except for July 7–13 with the westward wind. Since the measurements at different sites were not made simultaneously, the advection effects were not easily be removed from the raw data to provide snapshots of the horizontal distribution of physical and biogeochemical variables during the river flood period. A coupled physical Finite-Volume Community Ocean Model (FVCOM) and biogeochemical European Regional Seas Ecosystem Model (ERSEM) system was used to quantify the effects of the flood and TGD regulation on the physical and biogeochemical environments of the CE–ECS continuum.

FVCOM is a prognostic, unstructured-grid, finite-volume, free-surface, three-dimensional primitive equations model (Chen et al., 2003a, 2013). This model provides accurate geometric fitting for irregular coastlines and bathymetry, and solves the governing equations with high precision. It contains various modules for comprehensive physics, such as flows, waves, sediments in the coastal ocean, and specifically designed river boundary algorithms that connect the estuary and ocean to the drainage basin in the land. The ERSEM is a generic, most comprehensive, and established ecosystem/biogeochemical model for the lower trophic food web (Butenschön et al., 2016). This model includes pelagic and benthic components of marine ecosystems, such as microbial food webs, carbonate systems, and calcification. Four phytoplankton groups were considered in the pelagic system, including picophytoplankton, nanophytoplankton, microphytoplankton, and diatoms. Three groups for heterotrophic production were accounted for in the zooplankton pool, including nanoflagellates, microzooplankton, and mesozooplankton. The phosphate, oxidized nitrogen, ammonium, and silicate are major nutrients in the ERSEM (Butenschön et al., 2016). FVCOM–ERSEM coupling was done through the Framework for Aquatic Biogeochemical Models (FABM) developed by Plymouth Marine Laboratory (Bruggeman and Bolding, 2014).

The ERSEM model used in this study is configured with the same parameters as those specified in Ge et al. (2020a) and Ge et al. (2020b). Details are described in Fig. S1 of Supplement Material. The FVCOM and ERSEM shared the same spatial discretization with the non-overlapped unstructured triangular grid shown in Fig. 1b. The model grid covered the CE and inner shelf of the ECS. The model grid was expanded landward in the Changjiang River with a boundary reaching the Datong station. The horizontal grid resolution was ~500 m in the river channel and ~1–2 km in the river mouth. The time integrations for FVCOM and ERSEM also shared the same time step of 60.0 s. The coupled FVCOM-ERSEM system was driven by multiple forcings, including tidal elevation, winds, and freshwater discharges. The lateral boundary conditions were specified by physical and biogeochemical transports from the regional FVCOM model. The computational domain for the regional FVCOM model covered the Changjiang Estuary, East China Sea, Yellow Sea, Bohai Sea, Taiwan Strait, Japan Sea, and Northwest Pacific (Chen et al., 2008a; Ge et al., 2020a). The regional FVCOM model is driven by astronomical tide elevations predicted by the harmonic constants of tide constituents from Global Tidal Solution (Egbert and Erofeeva, 2002), subtidal flows from daily Global 1/12° Analysis data of the HYbrid Coordinate Ocean Model (HYCOM) prediction system (www.hycom.org). The upstream river boundary condition for the local estuarine FVCOM model was specified by daily freshwater and sediment discharges at the Datong station and the monthly-averaged concentrations of observed nitrate, phosphate, and silicate. Meanwhile, carbonate bio-alkalinity (CBA), total alkalinity (TA), and carbonate total dissolved inorganic carbon (DIC) were assumed to be constant at the boundary, which was 2.50 μmol/kg for CBA, 2065.0 μmol/kg for TA, and 2200.0 mmol C/m^3 for DIC.

The sea surface conditions encompassed the wind stress and net hear flux plus the vertical profiler of shortwave irradiance. These meteorological forcing data were constructed using the three-hour reanalysis product of the European Centre for Medium-Range Weather Forecasts (ECMWF). Additionally, the SST nudging assimilation was conducted for the regional FVCOM model. The SST data were from the Group for High-Resolution Sea Surface Temperature (https://podaac.jpl.nasa.gov/GHRSST) product with a 0.011° resolution. The wave and sediment modules were activated to simulate the suspended particulate matter (SPM), which was taken into account for light attenuation in the biogeochemical process throughout the water column. It should be noted here that the adsorption/desorption behavior of nutrients in SPM, particularly for phosphorus, were not included in the coupled FVCOM-ERSEM.

The water displacement under the fluvial flood wave was tracked using an offline Lagrangian particle tracking model developed originally by Chen et al. (2003c) and upgraded by Huret et al. (2007) and Chen et al. (2008b). The position of a water body was determined by a three-dimensional Lagrangian tracking equation given as

$$P_n\left(\vec{x}_{t+\Delta t}, t+\Delta t\right) = \int_t^{t+\Delta t} (\vec{v} + \alpha\vec{w})dt + P_n\left(\vec{x}_t, t\right) \quad (1)$$

where $P_n\left(\vec{x}_{t+\Delta t}, t+\Delta t\right)$ and $P_n\left(\vec{x}_t, t\right)$ are the locations of the nth individual water particle at the time of $t+\Delta t$ and t, $\vec{v}$ is the three-dimensional velocity vector from the FVCOM model, $\vec{w}$ is the surface wind vector that affects the water particle flows, α is the wind drag factor in the tracking and was set as 0.03 (Chen et al., 2012). The Lagrangian tracking was calculated with a fourth-order Runge–Kutta time-stepping scheme with second-order accuracy (Chen et al., 2013). This tracking model was driven by the FVCOM hourly flow field with horizontal and vertical diffusion coefficients for random walk parametrizations.

The model used in this study was initialized with a "hot-start" mode on June 1, 2016. The initial and boundary conditions for "hot-start" were produced by the model output at 00:00:00 GMT June 1, 2016 for an 18-year simulation over 1999–2016 (Ge et al., 2020b).

2.4. Model experiments

Three model experiments were performed in this study. The models were driven by the same external surface forcing for all experiments, including wind stress and heat flux, and open boundary conditions. The only difference was in the river discharge. For Experiment I (Exp-I), the model was run with daily freshwater discharge recorded at the Datong station. We referred to this experiment as a "realistic scenario." In this scenario, the maximum flood rate reached 7.1×10^4 m^3/s on July 11. For Experiment II (Exp-II), the model was run with a July climatologically averaged freshwater discharge of 5.0×10^4 m^3/s. This rate was calculated based on the monthly mean averaged over 1946–2019. Exp-II was referred to as the "climatological scenario," representing a non-flood scenario. For Experiment III (Exp-III), the model was run with the same freshwater discharge as that for Exp-I but withdrawing the water amount regulated by the TGD. Exp-III was viewed as the "non-TGD" scenario. In this case, the freshwater discharge was reduced by an amount of 2.5×10^4 m^3/s. After subtraction, the total runoff rate at the Datong station was 9.57×10^4 m^3/s. The daily runoff rates used in these three experiments are shown in Fig. 2.

2.5. Statistical analysis method

The coupled hydrodynamic-ecosystem model skills were evaluated via in-situ measurement data using the Taylor and Target diagrams. The Taylor diagram quantifies the correlation coefficient, standard deviation, and the centered root mean square error (CRMSE) between simulated and observed results (Taylor, 2001; Tian, 2019). Since the Taylor diagram may fail to identify some potentially essential aspects in coupled model performance, especially in the biased estimator. The additional Target diagram was applied to summarize the pattern statistics, bias, and the total Root-Mean-Square Difference (RMSD) (Jolliff et al., 2009). The RMSD was represented by the color of scatter points, where the systematic deviation was the standard deviation of the difference between simulated and observed mean values, i.e.,

$$B^* = \frac{\overline{m} - \overline{r}}{\sigma_r} \tag{1}$$

where B^* is a total bias between observed and model data; $\overline{m}$ and $\overline{r}$ are the mean values of simulated and observed data, respectively; $\sigma_r = \sqrt{\frac{1}{N-1}\sum_1^N (o_i - \overline{o})^2}$ is the standard deviation of observed data; and $\sigma_m = \sqrt{\frac{1}{N-1}\sum_1^N (m_i - \overline{m})^2}$ is the standard deviation of the simulated data. The correlation coefficients of each variable between simulated and observed data is defined as:

$$\rho = \frac{C_{mo}}{\sqrt{\sigma_r{}^* \sigma_m}} \tag{2}$$

where C_{mo} is the covariance between observed and simulated data. The unbiased root-mean-square is defined as:

$$RMSD^{'} = \sqrt{\frac{1}{N}\sum_{n=1}^{N}[(m_n - \overline{m}) - (r_n - \overline{r})]} \tag{3}$$

where N is the record number of each variable, m_n and r_n are the corresponding values. Based on the linear correlation coefficient $R = \frac{\frac{1}{N}\sum_{n=1}^{N}(m_n - \overline{m})(r_n - \overline{r})}{\sigma_m \sigma_r}$ and the normalized standard deviation $\sigma^* = \frac{\sigma_m}{\sigma_r}$, the unbiased root-mean-square in normalized standard deviation units is determined by $RMSD^{*'} = \sqrt{1 + \sigma^{*2} - 2\sigma^* R}$. The only positive normalized RMS error used the space of $X < 0$ regions.

Comparing the standard deviations of the simulated and observed data given as

$$\sigma_d = sign(\sigma_m - \sigma_r), \tag{4}$$

We drew a figure with $RMSD^{*'}\sigma_d$ on the x-axis and B^* on the y-axis. The scatter color presents the normalized total RMS error, low in blue and high in red. According to the above definition, the closer the scatter point is to the center, the more accurate the simulated results will be. Besides, the point's position was used to evaluate whether an overall error caused the difference between simulated and observed data.

3. Results

3.1. Observational results

The pre-flood survey, carried out on July 4–15, recorded that the runoff peaked at 7.0×10^4 m^3/s on July 12 at the Datong station. Since it took 5–7 days for the flood wave to travel over a ~650 km distance from Datong station to the channel region near the site C1, the CE–ECS continuum was under a non-flood condition. During this non-flood impacted period, the river channel and CE–ECS continuum were filled with fresher water, forming a low-salinity plume around the river mouth and inner shelf (Fig. 3a). This low-salinity plume exhibited an eastward extension pattern. In July, the salinity was lower in the CE–ECS continuum, varying in a range of 24–30 PSU. The SPM concentration was high in the river mouth and relatively low in the offshore shelf region (Fig. 3c). The maximum SPM concentration exceeded 500 mg/L in the maximum turbidity area. Nutrient concentrations had a similar distribution pattern as that of salinity, showing the dilution process from the river channel to the ECS inner shelf (Fig. 3d–f). The maximum concentrations of dissolved inorganic nitrate, phosphate, and silicate were 130 μM, 2.0 μM, and 120 μM, respectively. These variables exhibited evidence of a northeastward expansion, as they were diluted following the low-salinity plume. However, the *Chl a* concentration showed a much more complex distribution pattern, high in the inner shelf and northern coastal region and low or even vanished in the river channel, river mouth, and eastern open sea near 124°E (Fig. 3g). This pattern was closely related to SPM, nutrient concentrations, and tide-induced vertical mixing. High SPM concentration in the river channel and mouth reduced light penetration and restrained phytoplankton growth (Fig. 3c), even though nutrient concentrations in the river channel and mouth were sufficient. In the offshore region, the low *Chl a* concentration was mainly caused by inadequate nutrient supply, where dissolved inorganic phosphate and silicate concentrations were nearly zero (Fig. 3e-f). The maximum *Chl a* concentration was 28 mg/m^3, occurring outside of Hangzhou Bay. Additionally, three *Chl a* patches were observed along the outer edge of the low-salinity plume. The DO concentration near the surface was higher than the critical value for hypoxia, which was >4 mg/l in the region from the CE to the ECS inner shelf, with a maximum of >8 mg/l (Fig. 3h).

Meanwhile, dense contour lines of all near-bottom physical and biogeochemical variables located in the river mouth during the non-flood period (Fig. 4). The low-salinity water was mainly trapped in the shallow coastal region (Fig. 4a), with its position identical to the location where the maximum suspended sediment concentration (SSC) of >400 mg/L was observed (Fig. 4c). The nitrate and silicate had a similar structure as salinity (Fig. 4d, f), showing a dilution process dominated in the coastal region. However, the phosphate concentration was relatively low and uniform in the region (Fig. 4e). The *Chl a* concentration was relatively low (<4 mg/m^3) near the bottom (Fig. 4g). The bottom water experienced a low-DO environment with a concentration of <2 mg/L, indicating hypoxia in the northern (Fig. 4h).

The second survey captured the flood-induced substantial changes in physical and biogeochemical environments in the CE–ECS continuum (Fig. 5). The low-salinity plume was pushed strongly northeastward: The contour line of 24 PSU was shifted eastward to 124°E and northward to 32.5°N (Fig. 5a). The enclosed area of the 24 PSU contour line covered a major part of the study area. The maximum SPM concentration near the surface was significantly decreased throughout the region. In the maximum turbidity zone, it dropped from 500 mg/L before the flood to

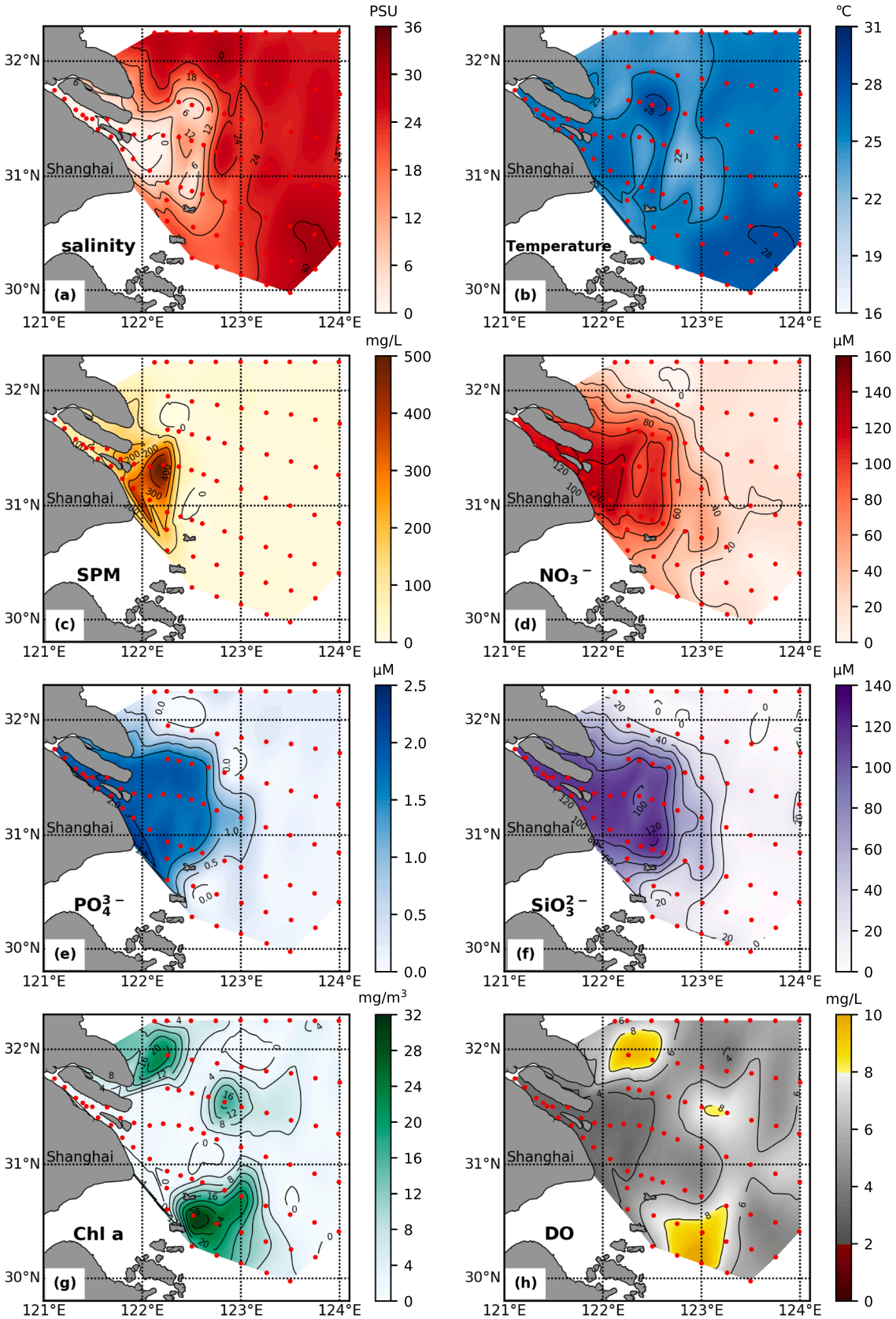

Fig. 3. Distributions of observed near-surface salinity (a), temperature (b), suspended particulate matter (SPM) (c), nitrate (d), phosphate (e), silicate (f), chlorophyll-a (*Chl a*) (g), and dissolved oxygen (DO) (h) on July 4–15, 2016 before the river flood.

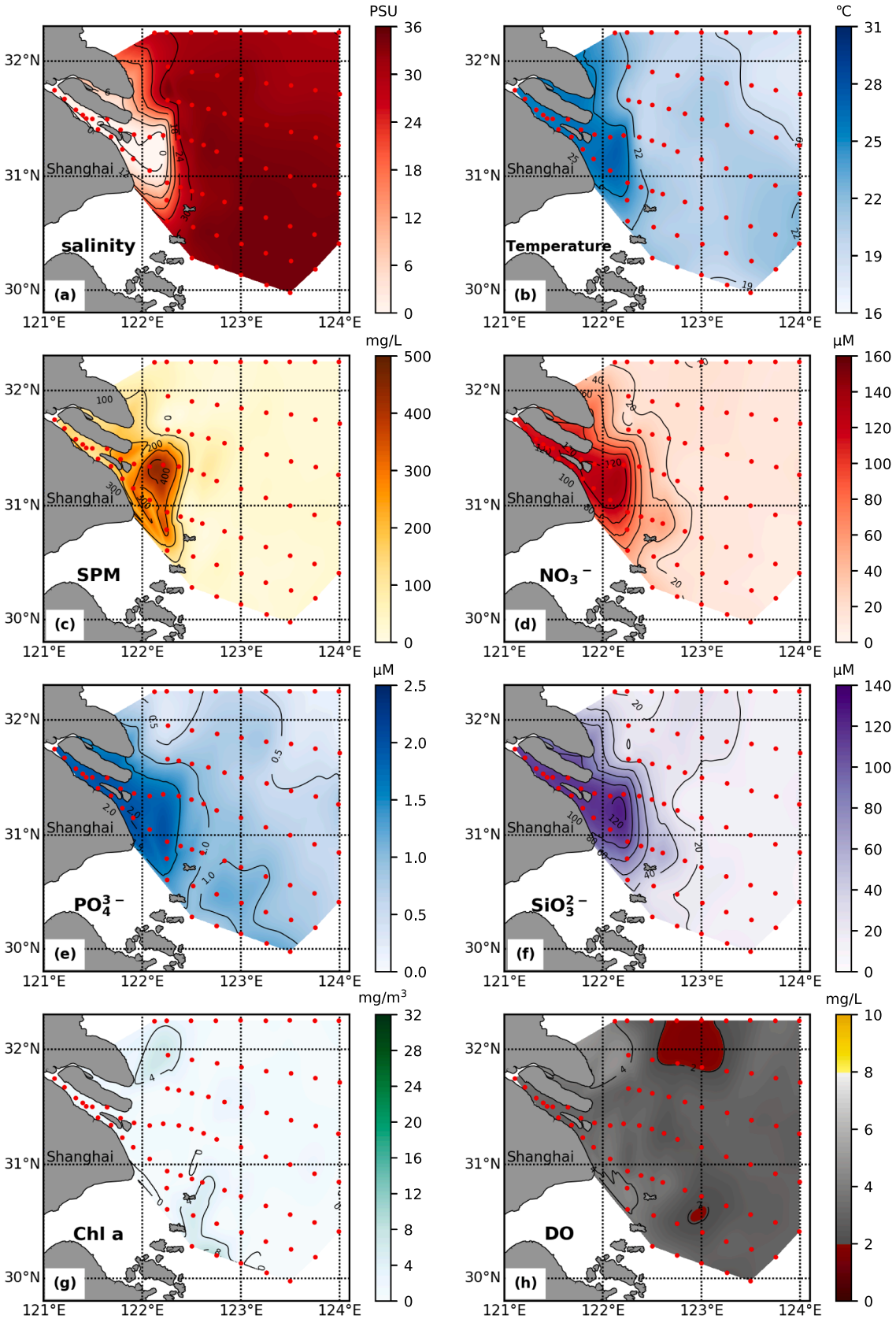

Fig. 4. Distributions of observed near-bottom salinity (a), temperature (b), suspended particulate matter (SPM) (c), nitrate (d), phosphate (e), silicate (f), chlorophyll-a (*Chl a*) (g), and dissolved oxygen (DO) (h) on July 4–15, 2016 before the river flood.

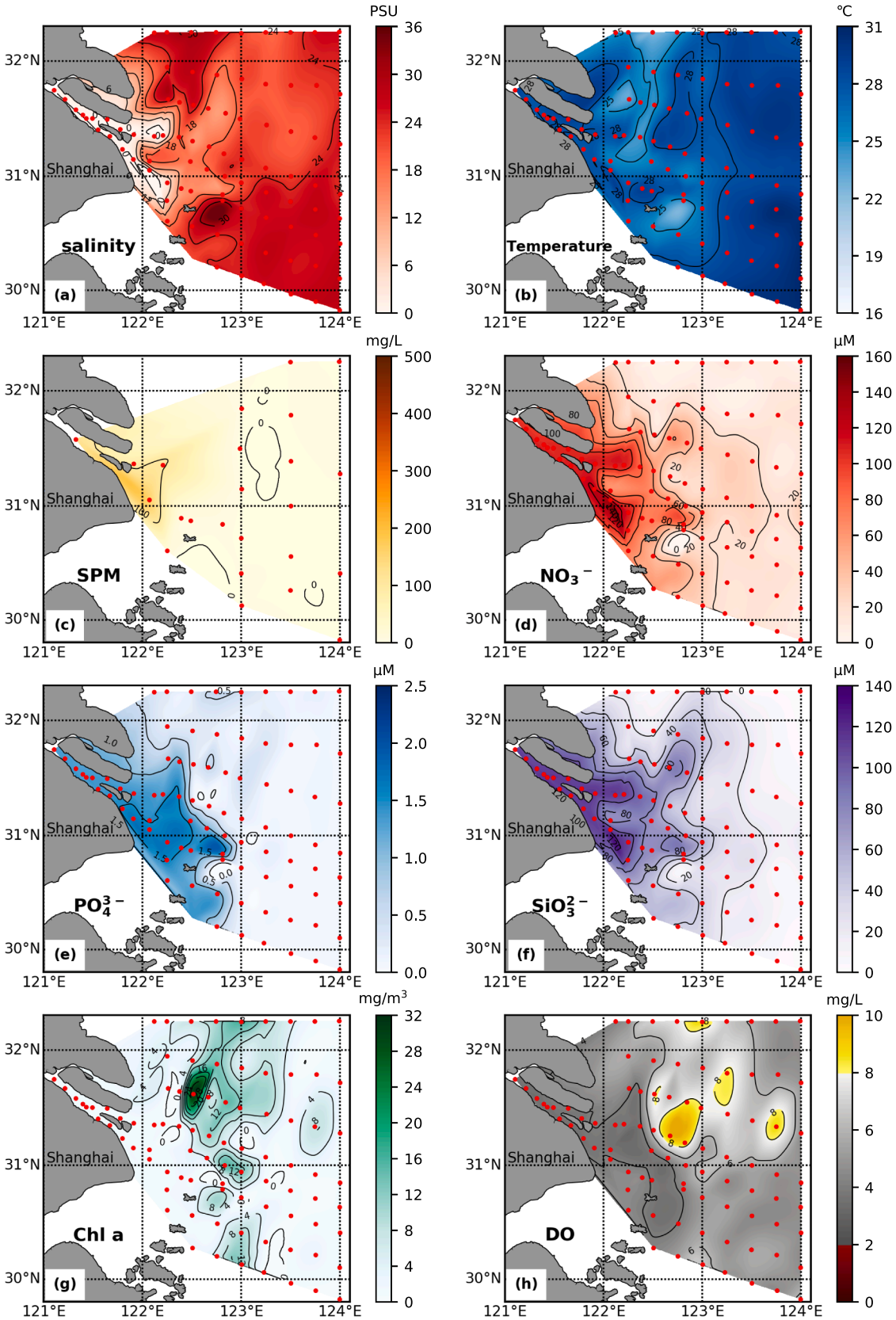

Fig. 5. Distributions of observed near-surface salinity (a), temperature (b), suspended particulate matter (SPM) (c), nitrate (d), phosphate (e), silicate (f), chlorophyll-a (*Chl a*) (g), and dissolved oxygen (DO) (h) on July 19–28, 2016 after the river flood.

~150 mg/L after the flood (Fig. 5c).

The dissolved inorganic nutrients were diluted in the river mouth and advected northeastward following the low-salinity plume (Fig. 5d–f). The maximum concentrations of nitrate and phosphate decreased to 100 μM and 1.5 μM, respectively, but the maximum silicate concentration remained at 120 μM, even though its area shrunk significantly. As for other nutrients, a notable offshore extension was evident for silicate (Fig. 5f). The influence of the river flood on the *Chl a* concentration was much more complicated than salinity and nutrients. It showed a notable eastward extension, with a patchier distribution in the CE–ECS continuum, particularly in the outer shelf region (Fig. 5g). The highest *Chl a* concentration was 28 mg/m^3, occurring in an area around 122.5°E and 31.5°N along the low-salinity plume extension path. The high *Chl a* concentration coincided with high nutrient concentrations around the extension tongue (Fig. 5d–f). The adequate supply of nutrients and optimal light provided favorable physical and biogeochemical conditions for phytoplankton growth and its induced algal blooms in that area. The northeastward displacement of high-DO water near the surface probably did not result from flood-induced transport. It is simply due to oxygen production by phytoplankton, therefore they are spatially aligned with *Chl a*. (Fig. 5h).

Compared with the pre-flood condition, the salinity, nitrate, phosphate, and salinity near the bottom remained little changed after the flood (Fig. 6a, d–f). As a result, no significant growth was observed in phytoplankton, with a low *Chl a* concentration as before (Fig. 6g). A significant difference occurred in SPM and DO (Fig. 6c and h). The SPM concentration decreased by about 100–200 mg/L in the river mouth after the flood. The DO significantly reduced, with a low concentration of ~4 mg/L or less everywhere. Hypoxia, defined as DO < 2 mg/L, occurred in the offshore area of the salinity plume, with an area of 3,286 km^2. The hypoxia was also observed around the river mouth during the first survey (Fig. 5h). The river flood pushed the salinity plume offshore, which enhanced vertical mixing in and around the river mouth and intensified vertical stratification on the offshore side of the flood displacement region. It explains why the hypoxia area shifted offshore after the flood.

3.2. Model validations

Since the estuarine flow varies significantly with time and space, the model-data comparison was made simultaneously at the location where the measurements were made. The coupled FVCOM–ERSEM model provided a reasonable prediction for the salinity, temperature, SPM, phosphate, nitrate, and silicate in the CE–ECS continuum over both pre and post-flood periods (Fig. S2 of Supplement Material). The correlation coefficients for simulated and observed temperatures and salinities were >0.88, with a total normalized bias (B^*) of <3%. In the low-salinity area, the model overestimated the salinity, particularly during the pre-flood period. Although the model was configured with assimilation of SST measurements, which only affects and improves the temperature prediction at the sea surface layer, the temperature in the middle and bottom water column was still calculated through advection and diffusion. For temperature, the bias was in a range of 3–5 °C in the cold area and 1–2 °C in the warm place, which was mainly caused by model-data discrepancy in the middle and bottom layers. The correlation for simulated and observed SPMs was 0.61, with a total normalized bias of 17%. This bias was acceptable for the high-turbidity SPM simulation due to considerable uncertainty and variation in observations. The correlation coefficients for simulated and observed nitrates and silicates were >0.9, with a total normalized bias of <9%. The model significantly underestimated the phosphate concentration with a total normalized bias of 44%, even though the correlation coefficient between simulated and observed values was 0.7. The large error was due to insufficient phosphate measurements at the Datong station during the flood period.

The model performance statistics for Exp-I is summarized by a non-dimensional Taylor diagram (Fig. 7a). The correlation coefficient of all variables exceeded 0.8, except *Chl a*. The simulated and observed variables were in good agreement in terms of the standard deviation and root-mean-squared error. The comparisons were further evaluated using the Target diagram (Fig. 7b). Most of the variables were scattered in the circle with a radius of 1.0 for B^* and $RMSD^* \sigma_d$. The B^* and $RMSD^* \sigma_d$ values for salinity and temperature were located in the center, indicating the physical simulation was in a high confidence level. Consistent with the Taylor diagram, the Target diagram showed small standard deviations for nitrates and silicates, a high root-mean-square error for *Chl a*, and a positive bias for phosphate. Previous observations revealed that phytoplankton moved up and down with a high-frequency vertical migration speed in a 1.0-m water layer near the surface (Lou and Hu, 2013). The relatively poor skill of *Chl a* is due to the inability of the model accurately represent the small regions where *Chl a* is high, as the model seems to indicate more consistent concentrations across large areas, rather than resolve small patches of *Chl a* blooms. Both diagrams demonstrated that the FVCOM-ERSEM model agreed well, in general, with observations during pre and post-flood survey periods.

The Taylor Diagram, Target Diagram and scatter plot between simulated and observed results mainly serve for general assessment of modeling skill, but do not allow a more precise understanding of the model realism. In order to understand the spatial and temporal sources of model errors, the distributions of observed values superimposed with simulated results before and after the fluvial flood were provided in Figs. S3–S6 in Supplemental Materials. They demonstrated the modeling results made good predictions for salinity, temperature, SPM, nitrate, phosphate and silicate for both near-surface and near-bottom layers. The simulated high-*Chl a* patch mainly located in the middle region of study area, rather than south region in first observation. The predicted coverage of surface *Chl a* matched well with second observation with smaller magnitude. The model generally predicted the surface DO in both two observations, however, the bottom hypoxia was not well resolved by model, showing similar location of low DO concentration, but the minimal DO concertation was 2–4 mg/L in modeling results. The modeled hypoxia was located in the south region (Fig. S6-h in Supplemental Materials).

3.3. Spatial impacts

Comparing the results among Exp-I, Exp-II, and Exp-III provided insights into the differences in spatiotemporal changes of the biophysical fields under climatological, realistic, and non-TGD scenarios. The Exp-I results show that the flood-induced maximum offshore expansion of the physical field in the CE–ECS continuum occurred on July 21, nine days after the flood peak wave was observed at the Datong station on July 11. We selected July 21 as a day for the three case comparisons. Taking Exp-I as a standard case, we examined the changes by examining differences between Exp-I and either Exp-II (climatological) or Exp-III (non-TGD regulation).

The Exp-I shows that the flood caused the low-salinity plume to expand northeastward and eastward (Fig. 8a). The simulated temperature was >28 °C in the river channels and coastal region and decreased to ~22 °C in the offshore area (Fig. 8b). High-turbidity was primarily constrained in the shallow region, with a depth-integrated value of >5 kg/m^2. The SSC was high inside the estuary and decreased sharply offshore in the deep water (Fig. 8c).

The difference between Exp-I and Exp-II shows that the flood caused a regional decrease in vertically averaged salinity, with a maximum decline around the river mouth (Fig. 8d). The expansion of the flood's influence area coincided with the seaward extension of the low-salinity plume, reaching the inner shelf at 124°E and 29.5°N within 10 days. It suggests that the river flood wave propagated rapidly, with a maximum salinity drop of >4.0 PSU around the river mouth. Meanwhile, the increased river flow produced a more substantial bottom shear stress, which significantly increased the SPM concentration in the river channel and mouth (Fig. 8f). Interestingly, the water temperature change was in

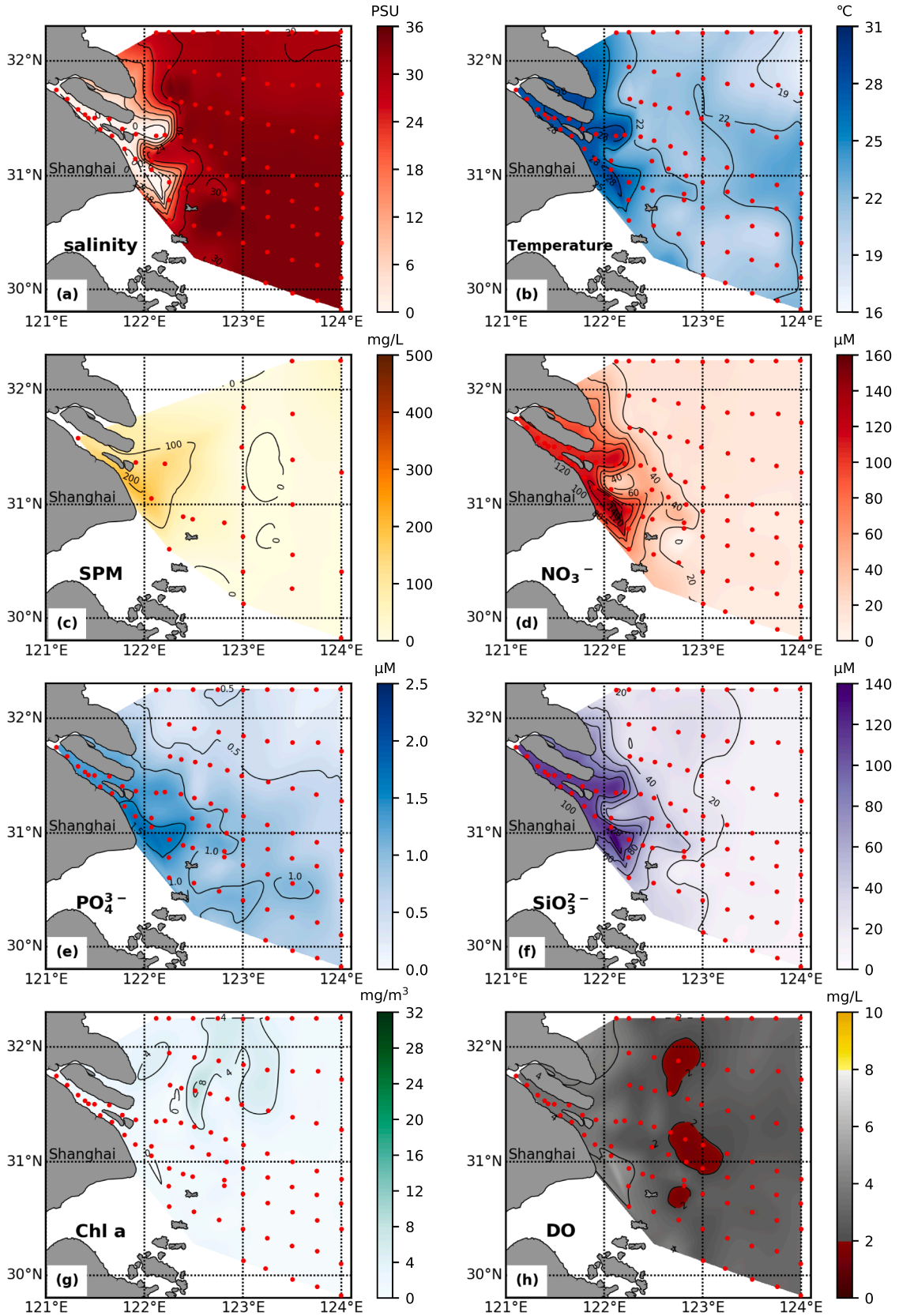

Fig. 6. Distributions of observed near-bottom salinity (a), temperature (b), suspended particulate matter (SPM) (c), nitrate (d), phosphate (e), silicate (f), chlorophyll-a (*Chl a*) (g), and dissolved oxygen (DO) (h) on July 19–28, 2016 after the river flood.

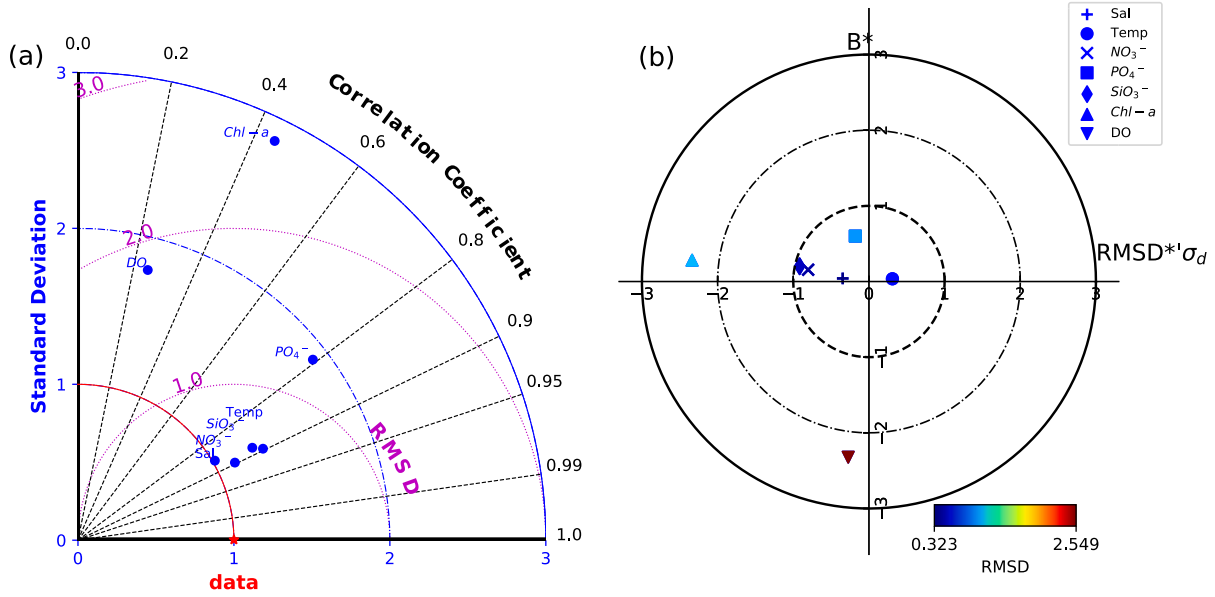

Fig. 7. Non-dimensional Taylor diagrams (a) and Target diagram (b) for salinity, temperature, nitrate, phosphate, silicate, and *Chl a*. Eighty-seven measurement sites made in July 2016 were included in the model-data comparisons.

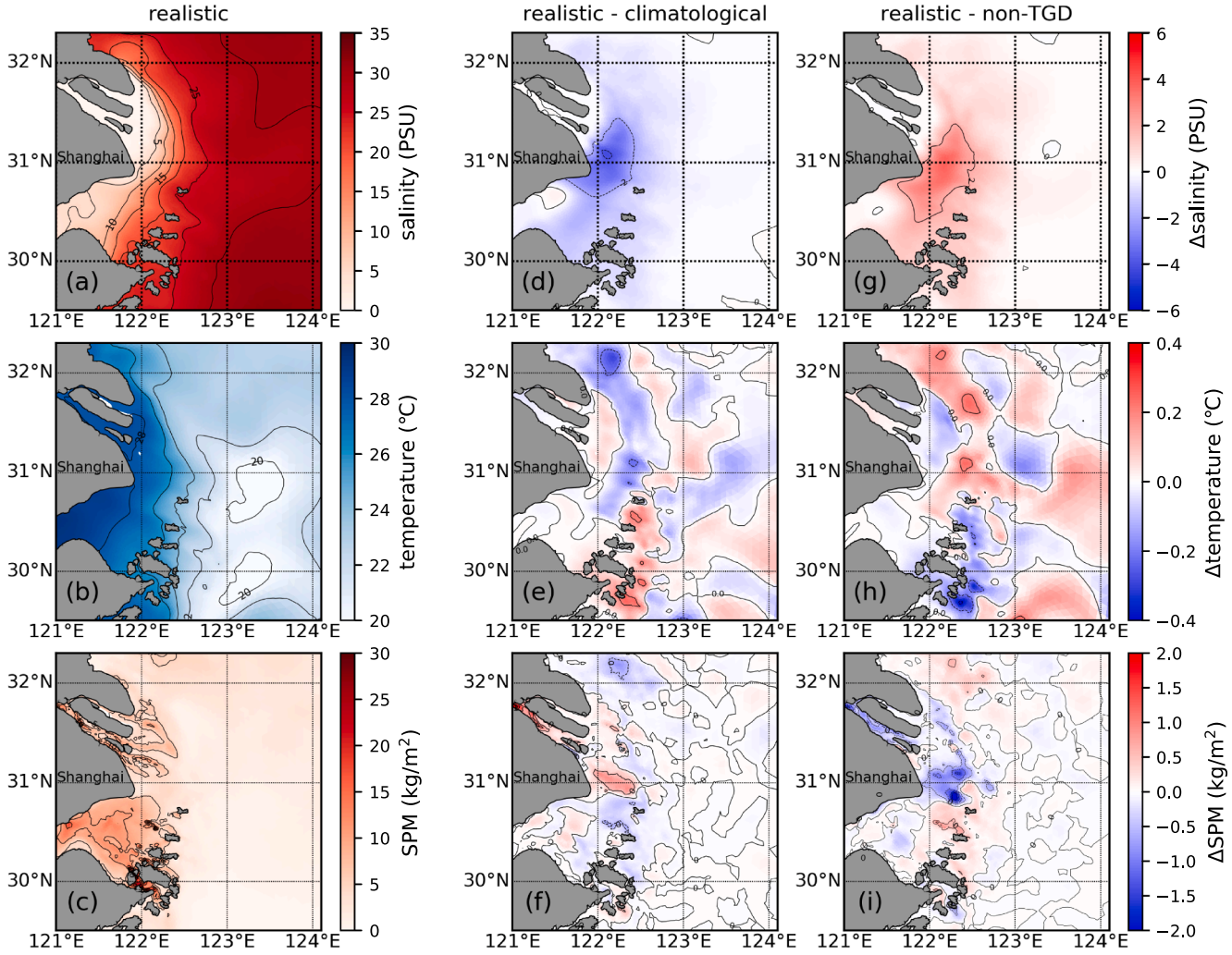

Fig. 8. Distributions of vertically-averaged salinity (first row) and temperature (second row), and vertically-integrated SPM concentration (bottom row) for Exp-I (left column), differences of these variables between Exp-I and Exp-2 (middle column), and between Exp-I and Exp-III (right column) on July 21, 2016.

a range of 0.2 °C, especially in the region from the river channel to the inner ECS shelf, where no significant temperature variation was found after the flood (Fig. 8e). The water temperature around the coastal and offshore areas was primarily controlled by the local solar irradiance, net surface heat flux, and wind and tidal-induced vertical mixing.

The comparison between Exp-I and Exp-III shows that the TGD regulation played a contradictory role via the flood (Fig. 8a–i). The TGD-reduced freshwater discharge was about 25,000 m^3/s, which was greater than the runoff difference between Exp-I and Exp-II. If this amount of the water entered the CE, it produced a positive salinity anomaly near the surface in the expanded area, even though the salinity anomaly distribution did not change (Fig. 8g). Similar to the Exp-I and Exp-II difference, the near-surface temperature difference between Exp-I and Exp-III was insignificant, with a change of <0.4 °C., However, the distribution of the near-surface temperature anomaly with the TGD regulation considerably differed compared with the climatological case (Fig. 8h). The near-surface SSC was controlled by the freshwater discharge, which was significantly reduced in the river channel and mouth in the case with the TGD regulation (Fig. 8i).

The comparison between Exp-I and either Exp-II or Exp-III demonstrates that the nutrients were like passive tracers to follow the low-salinity plume's eastward extensions (Fig. 9a). The Exp-I produced a high nutrient concentration zone in a deep submarine valley in the offshore area. In this area, the vertically-integrated nitrate and phosphate were >1.0 and 24 × 10^{-3} mol/m^2, respectively (Fig. 9a-b). The CE–ECS continuum features the phosphate-limited ecosystem (Chen

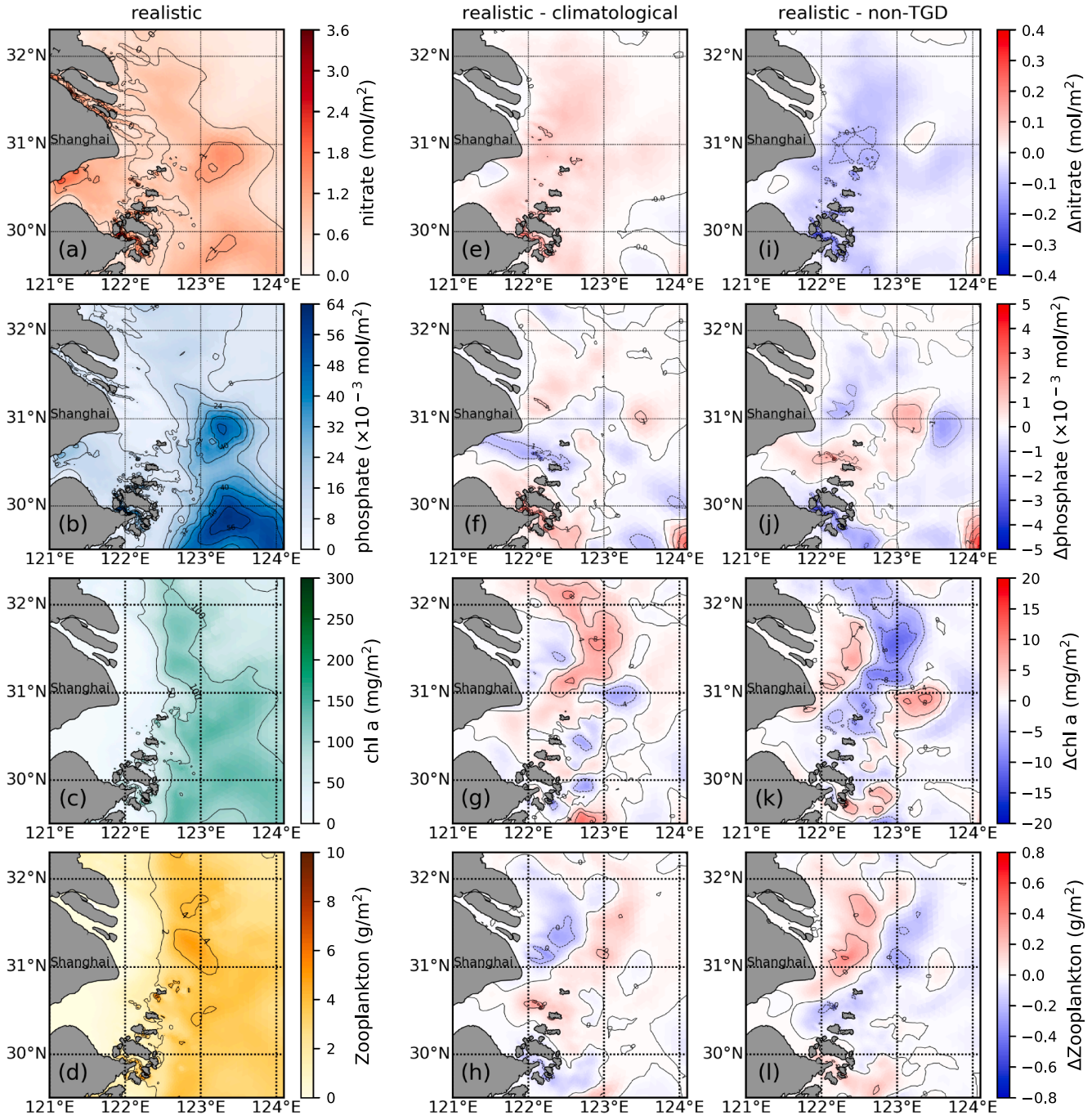

Fig. 9. Distributions of vertically-integrated nitrate (first row), phosphate (second row), Chlorophyll-a (*Chl a*; third row) and zooplankton concentrations (bottom row) for Exp-I (first column), differences of these variables between Exp-I and Exp-2 (middle column), and between Exp-I and Exp-III (right column) on July 21, 2016.

et al., 2003b). This result indicates that the flood shifted dissolved inorganic phosphate pool offshore to the deep submarine valley area, an intersection location of the river-diluted flow and northward Taiwan warm current (Chen et al., 2008a). This pool directly enhanced the autotrophic process, producing relatively high *Chl a* and zooplankton concentration zones in the offshore area (Fig. 9c-d). The maximum vertically-integrated *Chl a* and zooplankton concentrations were >100 mg/m^2 and 4 g/m^2 in that area (Fig. 9c-d).

The comparison between Exp-I and Exp-II suggests that the river flood significantly modified the local ecosystem after pushing the high phosphate pool offshore (Fig. 9e–h). The flood decreased nitrate concentrations in the river channel and produced a high nutrient concentration zone in the river mouth and over the shelf (Fig. 9e). The increase in the nitrate concentration was $>9.0 \times 10^{-2}$ mol/m^2 in the river mouth, with a cap of 5.0×10^{-2} mol/m^2 over the shelf (Fig. 9f). The changes in the phosphate concentration were similar to nitrate in the river channel but differed significantly from the river mouth to the shelf; high-concentration patches appeared around the outer edge of the low-salinity plume, with a maximum variation of approximately 1.0×10^{-3} mol/m^2 (Fig. 9f). In contrast, the flood significantly reduced the phosphate concentration in Hangzhou Bay. In this phosphate-limited ecosystem, the change in *Chl a* concentration coincided nicely with the flood-induced phosphate anomaly, decreasing in the river mouth and increasing in the offshore region, particularly in the northeastern area (Fig. 9g). The change in zooplankton was similar to *Chl a* (Fig. 9h), suggesting that the lower trophic food web dynamics in the CE-ECS continuum is a typical bottom-up ecosystem, in which an autotrophic process controlled the growth of phytoplankton.

The comparison between Exp-I and Exp-III demonstrates that TGD regulation resulted in an opposite effect on biogeochemical distributions. The flow increase without the TGD regulation caused an overall decrease of nitrate, with a maximum decline of $\sim 9.0 \times 10^{-2}$ mol/m^2 in the river mouth (Fig. 9i). It helped maintain phosphate in the river channel and reduced the phosphate increase rate in the river mouth and the shelf region (Fig. 9j). Meanwhile, a further offshore expansion of the low-salinity plume enhanced the flood impact on Hangzhou Bay and its adjacent areas. The phosphate concentration increases in those areas reached $\sim 1.0 \times 10^{-3}$ mol/m^2. The growth of phytoplankton was controlled nutrient uptake through photosynthesis. As the river flow increased without the TGD regulation, the phytoplankton and zooplankton increased in the river mouth and its adjacent northern region and decreased in the offshore area (Fig. 9k–l).

3.4. Temporal impacts

Sites A4-5 were located in the transient area of the CE–ECS continuum (Fig. 1b) and jointly influenced by fluvial discharge and ocean flow. We chose this site to highlight the temporal response of physical and biogeochemical variables to the river flood (Fig. 10). The three experiments started on June 1, and the river discharge for each scenario was added into the model on June 20 (black dashed line on the left in Fig. 2). The model results showed a significant difference in salinity (>0.2 PSU) among these three cases on July 1 (T1 in Fig. 10), suggesting that the flood wave traveled from Datong station to sites A4-5 over ten days. The runoff difference peaked on June 11 (T2 in Fig. 10), representing a 10-day delay. The maximum response occurred on June 21 (T3 in Fig. 10). That time was chosen for spatial analysis (Figs. 8 and 9).

In view of the physical environment, the salinity change in the CE–ECS continuum was mainly controlled by the mixing of river freshwater and ocean-intruded salty water. Since precipitation and evaporation were approximately balanced in the CE–ECS continuum (Chen et al., 1994), salinity could be treated as a conservative tracer as a first-order approximation. Our results showed that the salinity responses to the river flood and TGD regulation were rapid and lasted relatively long (Fig. 10a). The influence on salinity was evident even after the discharge adjustment stopped on August 19 (T4 in Fig. 10) since there were no significant salinity restoration signs at the end of August in the cases with and without the TGD regulation. Similarly, the dissolved inorganic nitrate concentration was relatively conservative (Fig. 10b). Previous studies and observations showed that nitrate was an excessive nutrient in the CE (Ge et al., 2020a; Gao et al., 2012; Shulkin et al., 2018; Yu et al., 2019). During the fluvial flood period, the ratio of nitrogen to phosphorus was 200 (~120 μM for nitrate, ~0.6 μM for phosphate).

On the other hand, dissolved inorganic phosphate and *Chl a* showed only a short-term response to the river flood (Fig. 10c-d). Phosphate was a primary limiting nutrient in the CE–ECS continuum (Chen et al., 2003b; Zhu et al., 2009). This limiting nutrient was positively correlated with phytoplankton growth. The flood-induced increase in phosphate concentration was quickly depleted by local phytoplankton. Both phosphate and *Chl a* varied significantly until the end of July. Subsequently, the simulated biogeochemical variables from the three experiments showed the same variations, suggesting that phosphate and *Chl a* were less affected by either the flood or TGD regulation. Zooplankton growth followed the change in *Chl a*. The grazing rate was proportional to the phytoplankton biomass. The zooplankton grew with the increase of *Chl a* (Fig. 10e). When the uptake of nutrients reached saturation, the maximum phytoplankton biomass occurred. The successive zooplankton grazing caused a decrease in phytoplankton biomass, and the maximum zooplankton biomass happened when the *Chl a* concentration reached a minimum (Fig. 10d). These features do not change under either climatological or non-TGD-regulation cases, implying that the river flood did not change the nature of the lower trophic feed web dynamics in the region.

However, the DO experienced a longer delay in response to the river flood, especially near the bottom (Fig. 10f). A rapid drop of DO concentration occurred on July 21, almost one month later, after the fluvial flood started. The DO was reduced by ~2.5 mg/L over ten days from July 21 to July 31, with a minimum of <2 mg/L occurring on August 1. After that, the DO experienced an increased period for about a week and remained at a level of ~4.5 mg/L during August 13–26. The three experiments all produced the same temporal variation of the DO concentration, except for distinct minimum values. The Exp-I predicted a minimum DO lower than 2.0 mg/L, with hypoxia lasting for a few days. The Exp-II predicted a slightly worse hypoxia scenario than the Exp-I, although the river discharge was $\sim 2.0 \times 10^4$ m^3/s less in the Exp-II case. With a more fluvial discharge from the non-TGD regulation case, the model-predicted minimum DO concentration was over 2.0 mg/L, which helped reduce the local hypoxia risk (Fig. 10f).

The temporal variations shown in Fig. 10 only reflected the change at local sites 4–5. For a broader area of the CE and inner shelf of ECS, the temporal response to the flood varied significantly with time and space (see Supplemental Materials S7-S9). Taking DO for an example, the Exp-I result suggested that hypoxia near the bottom was gradually developed with an increased spatial coverage over July 21–August 17 (Fig. 11 a–c), with a mainly covered area in an offshore region. Compared with Exp-II, the Exp-I simulation suggested that flood wave caused hypoxia in the offshore deep submarine valley on July 21 (Fig. 11d). This hypoxia condition became worse on August 8. In addition to a northward expansion of the low-DO area in the valley, the DO outside of the river mouth turned into a hypoxia condition (Fig. 11e). The hypoxia remained on August 17, even though several spots disappeared or shrank (Fig. 11f). The comparison between Exp-I and Exp-III results shows that the case with and without the TGD regulation produced opposite spatial and temporal variations regarding the fluvial flood impacts (Fig. 11g–i).

3.5. Physical water displacement and stratification

Although the river flood caused strong remote responses from physical and biogeochemical variables (Figs. 8 and 9), it did not mean the flood water actually be transported there. These spatial responses were mainly caused by water-body shifting, which can be determined by the Lagrangian drifter tracking. Three drifters were deployed near the

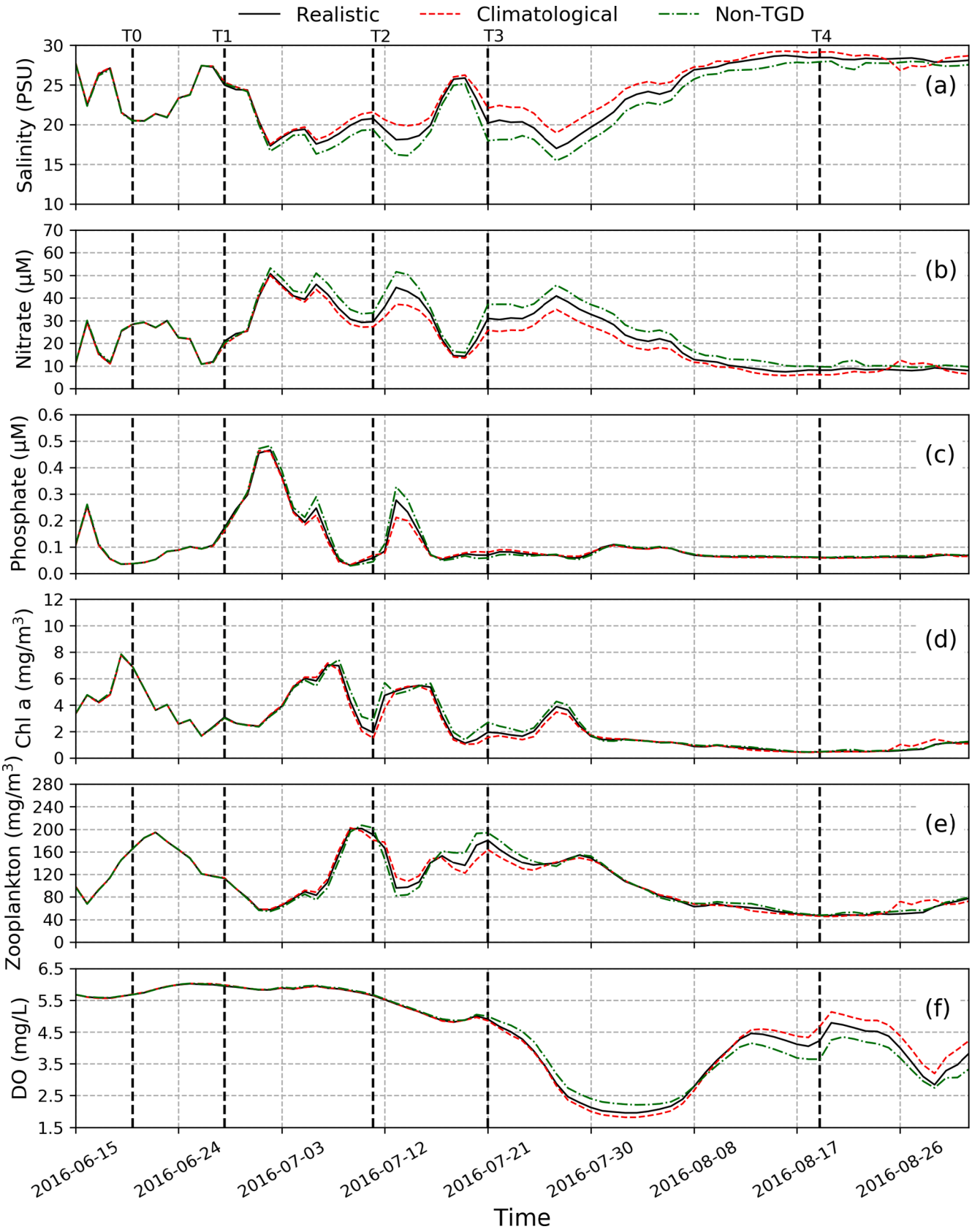

Fig. 10. Time series of near-surface salinity (a), nitrate (b), phosphate (c), *Chl a* (d), zooplankton biomass (e), and DO concentration (f) at site A4-5 for Exp-I, Exp-2, and Exp-3. T0-T4 indicates the time tags of June 20, June 28, July 11, July 21, and August 19.

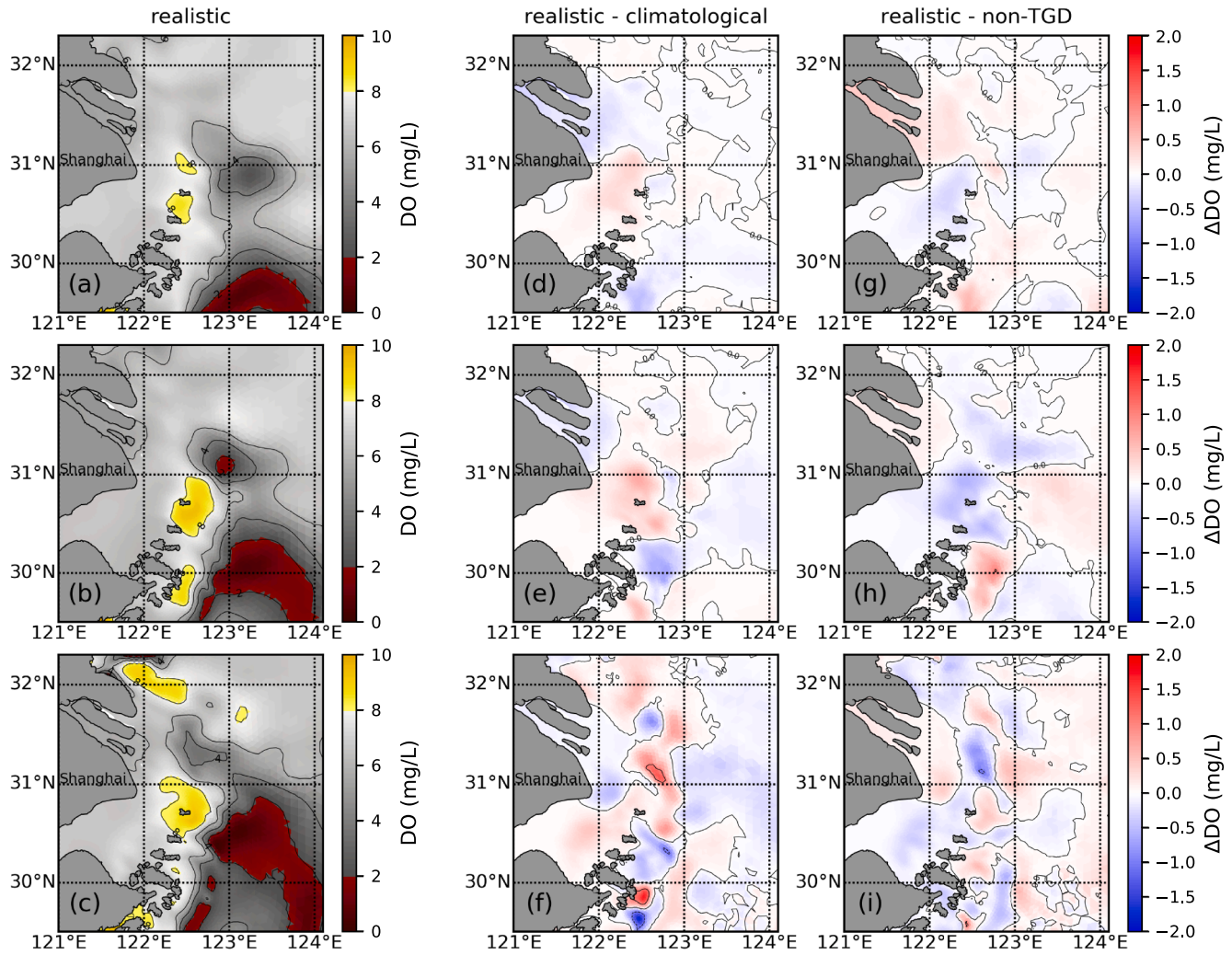

Fig. 11. Distributions of the near-bottom DO concentration at July 21 (left column: first row), August 3 (left column: second row), and August 17 (left column: bottom row). 2016, and the corresponded DO differences between Exp-I and Exp-III (middle column) and between Exp-I and Exp-III (right column). The filled dark red region bounded by a 2 mg/L contour represents the hypoxia coverage. (For interpretation of the references to color in this figure legend, the reader is referred to the web version of this article.)

surface (0.5-m deep) at the same location in the central river channel for Exp-I, Exp-II, and Exp-III, respectively (Fig. 12). These drifters were released at 0:00 AM, July 10, and exhibited noticeably different trajectories under different discharge conditions (Fig. 12). The results indicated the water could be pushed much further eastward. Under the flood conditions, the water showed more evident northeastern expansion. This pattern agreed well with the theory of Yankovsky and Chapman (1997). They pointed out that with a higher amplitude of river discharge, the radial distance from the center of the anticyclonic buoyant plume could be increased. Therefore, the flood could cause an enlarged radius of the anticyclonic buoyant plume and transport the water body to a much longer distance. Compared with Exp-II, the Exp-I can produce an additional water displacement by ~1° in the longitudinal direction. However, water displacement was not fully controlled by the amount of river discharge. The water displacement for the cases with and without TGD regulation had similar patterns in the radius and transport distance.

The river flood significantly changed water stratification in the CE–ECS continuum due to increasing freshwater discharge. This change was evident on an along-river transect from the river channel to the offshore region (dashed line in Fig. 1b). Before the river flood, the offshore area between A3-4 and A1-7 was dominated by salty and cold oceanic water except near the surface, while the estuarine region from C1 to B3 was mainly occupied by the fresher and warm riverine water (Fig. 13a-b). A density front appeared between these two water masses with a low-density area in the nearshore area between C1 and B3 and a high-density area in the offshore region between A3-4 and A1-7 (Fig. 13c). This surface-bottom density front tilted in the vertical, with its bottom edge at site B3 and surface outcrop at site A3-4. It clearly showed the offshore expansion of the low-salinity riverine water in the upper 5-m layer. The river flood enhanced vertical mixing inside the river channel and offshore low-salinity expansion in the upper 5 to 10-m layer. However, it did not significantly change the vertical profilers of the salinity and temperature in these two water mass regions. As a result, the density front slightly moved offshore, with a reduced tilted angle in the vertical. In the offshore area between site A3-4 and site A1-7, the near-surface water became much fresher, and the main thermocline at a depth of ~5–8 m was intensified (Fig. 13f). These changes can be viewed in the distribution of the density difference before and after the flood shown in Fig. 13g.

Therefore, the flood significantly intensified vertical stratification in the offshore region, resulting in a robust horizontal water displacement through conservative advection effects. The intensified stratification reduced reaeration through the air-sea interface and raised the hypoxia risk in the offshore regions.

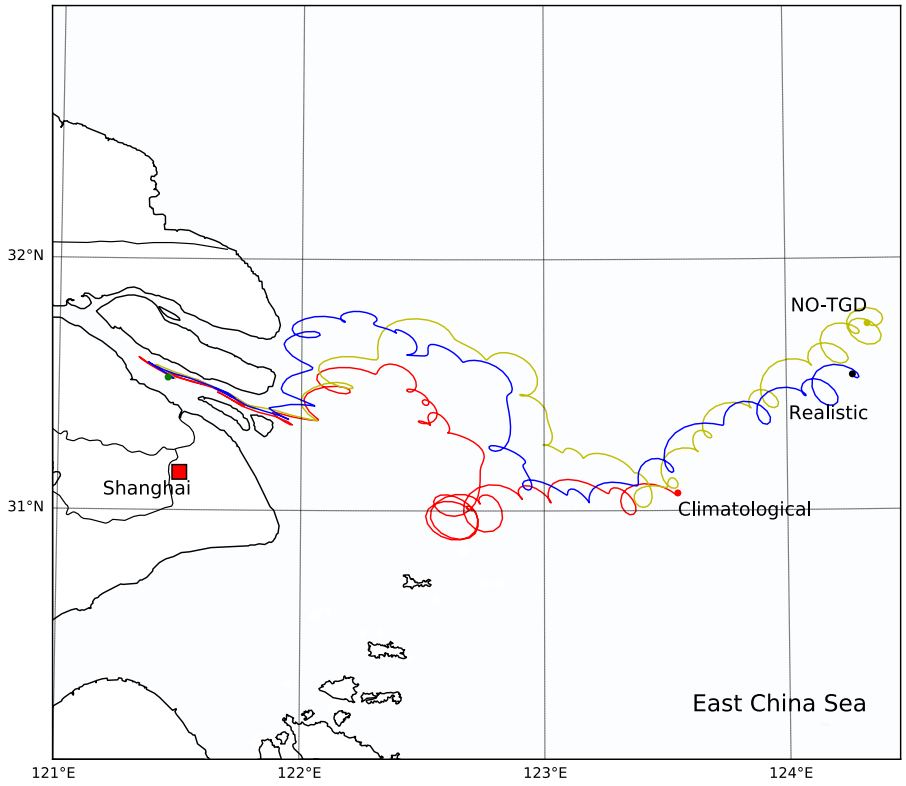

Fig. 12. Model-predicted surface drifter trajectories over July 10–23, 2016 for Exp-I (red), Exp-II (blue), and Exp-III (yellow). (For interpretation of the references to color in this figure legend, the reader is referred to the web version of this article.)

4. Discussions

4.1. Limitations and prospects

Two surveys provided us insights into flood-induced physical and biological changes along the CE-ECS continuum. However, since the measurements were mainly made along a longitudinal line inside the river, the observed data could not validate the coupled physical and biological model in terms of the lateral variation in the CE. To resolve the lateral structure, one is required to make high-resolution measurements like those done in other estuarine regions using Continuous Plankton Recorder, Gliders, and Scanfishes (Voynova et al., 2017; Houghton et al., 2004; Reid et al., 2003).

Our FVCOM-ERSEM experiments did not consider the nutrient absorption/desorption by sediments, which might not be neglected for phosphorus in the sediment-dominant estuaries (Froelich, 1988; Davis and Kent, 1990). Pan et al. (2013) reported that in the Yellow River, China, the low-concentration sediment (<100 mg/L) was a phosphorus source in the ambient water, while the relatively high-concentration sediment acted as a nutrient sink to remove phosphorus through absorption. Chen et al. (2003b) revealed that the nutrient release from resuspended sediment becomes a cause of the near-bottom phytoplankton bloom in the CE. We believe that neglecting the sediment-induced nutrient absorption/desorption is the reason why the ERSEM showed a large total bias and lower correlation coefficient between simulated and observed phosphates (Fig. S2 in Supplemental Materials). Meanwhile, the assumption of constant SPM and nutrient concentrations at river boundary during flood seemed to work for Exp-I and Exp-II, but not for Exp-III. Previous observations revealed that the TGD retention-maintained dissolved nutrients were accounted for 15%, 12%, and 1% of the total nitrate, phosphorus, and silicates in the CE, respectively (Ding et al., 2019). These retention of nutrients and SPM concentrations were not taken into account for Exp-III. Therefore, the flood's impact on the local physical and biogeochemical dynamics in the CE-ECS continuum could be underestimated in this experiment.

The major discrepancy between the model and observations mainly occurred in *Chl a* and DO. The model underestimated the high value of small-area phytoplankton patches, tending to predict more consistent concentrations across large areas. In the field cruise, we noticed there were some small patches with high-concentration *Chl a* and significantly different visual ocean color from ambient water. There was obvious boundary between patches and ambient water. This pattern, however, is of great challenge to be well resolved in simulation. The formation and locations of these patches are fairly random. They were closely related to the small-scale dynamics of horizontal advection and diffusion. It probably requires a sub-grid model with weak mixing to capture this structure. Since the hypoxia is often associated with the overgrowth of certain species of algae, that results in oxygen depletion when they die, sink and decompose in the lower water column. The underestimation of phytoplankton growth can lead to weak oxygen depletion, consequently overestimation of DO concentration.

Our recent observations in the South Branch (C1–C5 section in Fig. 1) suggested the nutrients composition was significantly modified during the fluvial flood period, showing the nitrate was strongly increased and phosphorus was decreased (not shown in this study). Since the turbidity in the river channel was high, the phytoplankton growth is weak, as well as the depletion of nutrients (Figs. 3–6). The modification of nutrient composition should be mainly caused by upstream source from the fluvial flood. The nutrient modification had different behavior in various river system, depending on different catchment soil, primary production level and nutrient assimilation, even removal process (O'Mara et al., 2019; Talbot et al., 2018). Future observations should pay more attention to the nutrient composition in the river, specifically, the Datong station for the Changjiang Estuary. It also results in much more complicated biogeochemical response in the estuary and continental shelf region. Although the fluvial flood is a short-term event, the response of flood estuary-shelf continuum could be long-term. To quantify these effects, the numerical model system needs longer

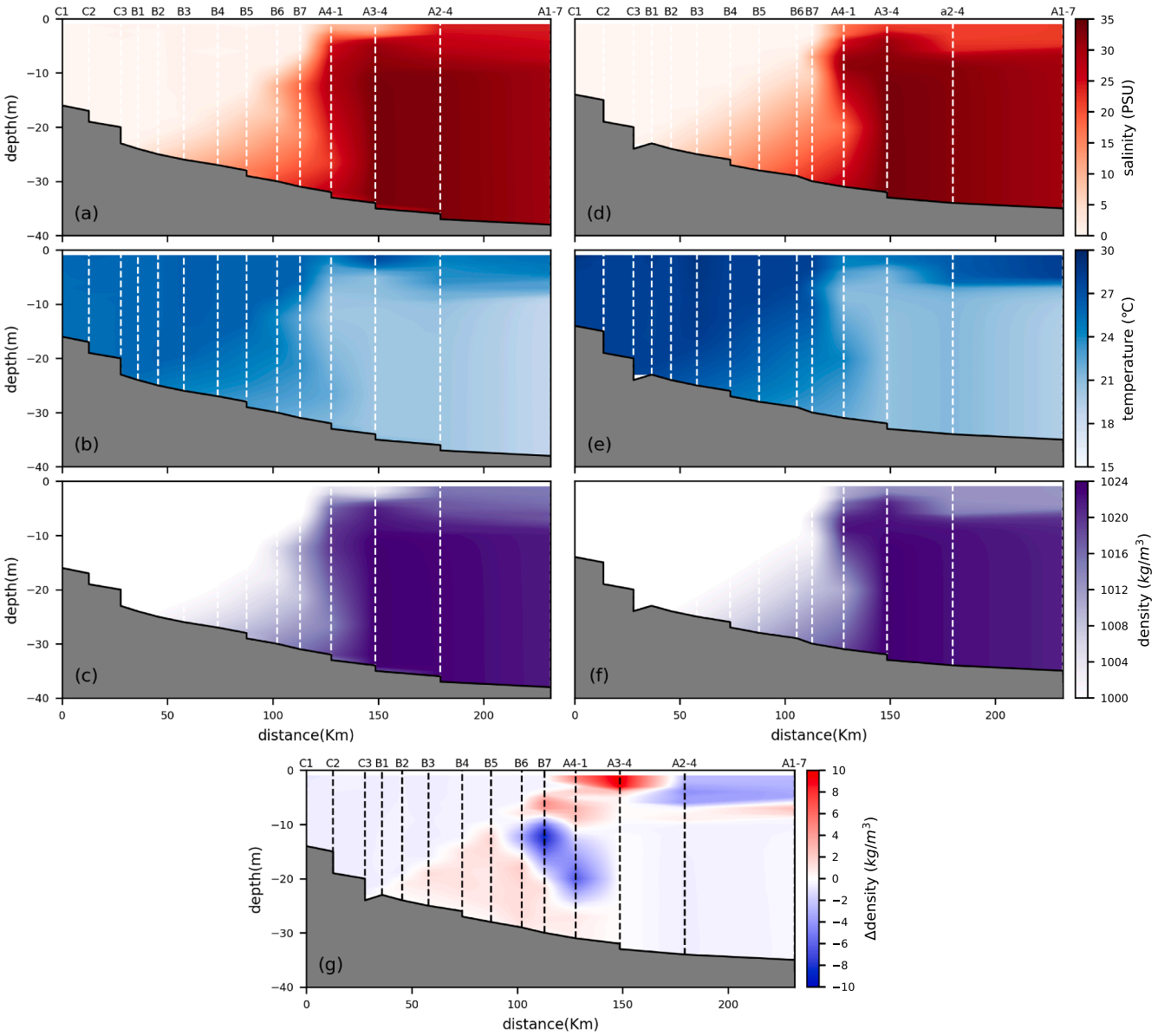

Fig. 13. Vertical distributions of salinity (top row), temperature (middle row), and density (bottom row) from the river channel to the offshore region for the first (a, b, c) and second (d, e, f) field surveys. The density difference between the two surveys is shown in (g).

simulation time in future study.

4.2. General consequences and implications

Similar water displacement was also observed during the Mississippi River flood period from the remote sensing images (Shi and Wang, 2009; Gierach et al., 2013). The flood caused a large-scale freshening in the Gulf of Mexico. With a river flood-induced freshwater discharge of ~4.0 $\times$ 10^4 m^3/s, the areal coverage of low-salinity plume was doubled (Shi and Wang, 2009). The low-salinity plume showed relatively persistent spreading, lasting about 1–3 months (Gierach et al., 2013). Similar findings in the CE and Mississippi River suggests that the river flood's impact has the same dynamic feature; a short-term flood event could result in a long-term residual impact on physical and biogeochemical fields over the inner shelf.

The river flood water carries abundant dissolved nutrients that could stimulate the phytoplankton biomass and boost algal blooms in the coastal and offshore regions (Gong et al., 2011; Voynova et al., 2017; Howley et al., 2018). The observational results confirmed that the phytoplankton-induced *Chl a* had broader scattering after the river flood (Fig. 5g). The Exp-I produced a high *Chl a* concentration around the offshore region (Fig. 9g). These results suggested a consequence of the ecosystem change in phytoplankton near the surface caused by the flood-induced surface horizontal water displacement.

On the other hand, the flood-induced change in the vertical structure of the salinity could also have a potential impact on biogeochemical processes. Long-term coverage of the low-salinity water increased the vertical stratification in the offshore region, which limited the upward nutrient transport from the lower water column, particularly for dissolved inorganic phosphate. It thus shortened the duration of the surface boost of phytoplankton growth (Fig. 10).

The hypoxia is a common near-bottom feature in the CE during the summer, which is mainly caused by oxygen depletion and organic matter decomposition (Zhu et al., 2011). We found that floods cause a much worse hypoxia condition in the region. In the CE–ECS continuum, natural and anthropogenic forcings cause the fluvial flood. However, under a flood condition, the biophysical environment is fully controlled by nonlinear interactions among tidal, winds, and freshwater

discharges.

Meanwhile, the enhanced stratification also constrained the downward dissolved oxygen (DO) transport from the sea surface to the bottom. Both our modeling results and remote sensing data analysis by Gierach et al. (2013) suggest that the flood-enhanced stratification is stable and persistent over a long time. The intensified vertical stratification could result in hypoxia near the bottom. Our finding was also consistent with previous studies in other estuaries reported by Voynova et al. (2017) and Talbot et al. (2018). They found that the river flood could lead to a possible lack of oxygen transport into the bottom water and soil under prolonged stratification. Depleting oxygen transport can cause deterioration of water quality in various estuaries. In addition to the flood, other physical factors, e.g., surface weather conditions, could also play an essential role in hypoxia development (Kerimoglu et al., 2020). The persisted hypoxia/anoxia around the river mouth and offshore region resulted in deleterious effects on benthic communities (Mallin et al., 2002) and caused fish and benthos mortalities (Paerl et al., 1998). Additionally, the survival and physiology of pelagic species such as prawns would also be affected by a rapid salinity change during flood events (Tyler et al., 2017). The river flood can potentially disturb the nursery's environment for aquatic species and benthos and consequently has a negative impact on fisheries.

5. Conclusion

To determine the impact of the river flood on physical and biogeochemical fields in the Changjiang River, two field surveys were carried before and after a significant flood with water regulation by the TGD in July 2016. The FVCOM–ERSEM coupled model was applied to simulate the observed variables. Three process-oriented modeling experiments were subsequently conducted to examine the spatiotemporal responses of salinity, nutrients, *Chl a*, and dissolved oxygen to the flood in the light of TGD regulation. Observational and modeling results revealed that the river flood caused significant northeastward expansions of salinity and dissolved inorganic nutrients and promoted the phytoplankton growth in the offshore region. It also increased the vertical stratification and consequently decreased the DO concentration. The TGD regulation shrank the low-salinity nutrient plumes toward the estuary, increased salinity, decreased the nutrient concentration, and suppressed the phytoplankton growth. However, the TGD regulation could increase the hypoxia risk in the offshore area. The responses of salinity and nitrate concentration mainly followed a conservative pattern, but phosphate and *Chl a* concentration showed noticeable patched anomalies in the shelf region. The conservative salinity and quasi-conservative nitrate concentration required a longer time to recover from the river flood and TGD regulation. In contrast, phosphate and *Chl a* concentrations had a shorter recovering time, showing higher resistance to the river flood. DO, however, experienced a delayed but persistent response to the flood or TGD regulation.

The major river flood also extensively modified the vertical structure of the salinity, particularly in the offshore region, enhancing water stratification. The intensification of stratification could be persistent due to the long-term low-salinity floodwater extension. It promoted significant deleterious effects on water quality, triggering or worsening the low-oxygen environment, even leading to hypoxia/anoxia. The deleterious and harmful water quality has a great potential to influence fisheries due to rapid and uninhabited changes of survival and physiology for pelagic and benthic communities. Although the river dams such as TGD were primarily designed for river flood defense, the river runoff modification could produce various short- and long-term impacts on the estuarine physical and ecosystem environments, especially after floods.

CRediT authorship contribution statement

Jianzhong Ge: Conceptualization, Methodology, Formal analysis, Investigation, Writing - original draft, Funding acquisition. **Jingsi Zhang:** Data curation, Writing - original draft, Visualization. **Changsheng Chen:** Formal analysis, Investigation, Writing - review & editing. **Pingxing Ding:** Supervision, Project administration, Writing - review & editing.

Declaration of Competing Interest

The authors declare that they have no known competing financial interests or personal relationships that could have appeared to influence the work reported in this paper.

Acknowledgments

This study was supported by the National Key R&D Program of China (grant no. 2016YFA0600903) and the National Natural Science Foundation of China (grant nos. 41776104; 41761144062). C. Chen was supported by the Montgomery Charter Chair fund at the University of Massachusetts-Dartmouth. The field survey was supported by NSFC Ship-time Sharing Project.

Appendix A. Supplementary data

Supplementary data to this article can be found online at https://doi.org/10.1016/j.jhydrol.2021.126441.

References

Butenschön, M., Clark, J., Aldridge, J.N., Allen, J.I., Artioli, Y., Blackford, J., et al., 2016. ERSEM 15.06: a generic model for marine biogeochemistry and the ecosystem dynamics of the lower trophic levels. Geosci. Model Dev. 9 (4), 1293–1339. https://doi.org/10.5194/gmd-9-1293-2016-supplement.

Bruggeman, J., Bolding, K., 2014. A general framework for aquatic biogeochemical models. Environ. Modell. Software 61 (C), 249–265. https://doi.org/10.1016/j.envsoft. 2014.04.002.

Chen, C., Beardsley, R.C., Limeburner, R., Kim, K., 1994. Comparison of winter and summer hydrographic observations in the Yellow and East China Seas and adjacent Kuroshio during 1986. Cont. Shelf Res. 14 (7-8), 909–929.

Chen, C., Liu, H., Beardsley, R.C., 2003a. An unstructured, finite-volume, three-dimensional, primitive equation ocean model: application to coastal ocean and estuaries. J. Atmos. Ocean. Technol. 20, 159–186.

Chen, C., Zhu, J., Beardsley, R.C., Franks, P.S., 2003b. Physical-biological sources for the dense algal bloom over the western shelf of the East China Sea. Geophysi. Res. Lett. 30 (10), 1515, 22–1:4.

Chen, C., Xu, Q., Beardsley, R.C., Franks, P.J.S., 2003c. Modeling studies of the cross-frontal water exchange on Georges Bank: a 3D Lagrangian Experiment. J. Geophys. Res. -Oceans 108 (C5), 8011. https://doi.org/10.1029/2002JC001358.

Chen, C.P., Xue, P., Ding, R.C., Beardsley, Q.X., Mao, X., Gao, G., Qi, J., Li, C., Lin, H., Cowles, G., Shi, M., 2008a. Physical mechanisms for the offshore detachment of the Changjiang diluted water in the East China Sea. J. Geophys. Res.-Oceans 113. https://doi.org/10.1029/2006JC003994. C02002.

Chen, C., Qi, J., Li, C., Beardsley, R.C., Lin, H., Walker, R., Gates, K., 2008b. Complexity of the flooding/drying process in an estuarine tidal-creek salt-marsh system: an application of FVCOM. J. Geophys. Res. 113, C07052. https://doi.org/10.1029/2007jc004328.

Chen, C., Limeburner, R., Gao, G., Xu, Q., Qi, J., Xue, P., Lai, Z., Lin, H., Beardsley, R., Owens, B., Carlson, B., 2012. FVCOM model estimate of the location of Air France 447. Ocean Dyn. 62 (6), 943–952. https://doi.org/10.1007/s10236-012-0537-5.

Chen, C., Beardsley, R.C., Cowles, G., Qi, J., Lai, Z., Gao, G., Stuebe, D., Liu, H., Xu, Q., Xue, P., Ge, J., Ji, R., Hu, S., Tian, R., Huang, H., Wu, L., Lin, H., Sun, Y., Zhao, L., 2013. An unstructured-grid, finite-volume community ocean model FVCOM user manual. In: SMAST/UMASSD Technical Report-13-0701, 3rd ed. University of Massachusetts-Dartmouth, p. 404.

Chen, C.C., Gong, G.C., Chou, W.C., Chung, C.C., Hsieh, C.H., Shiah, F.K., Chiang, K.P., 2017. The influence of episodic flooding on a pelagic ecosystem in the East China Sea. Biogeosciences 14 (10), 2597–2609. https://doi.org/10.5194/bg-14-2597-2017.

Davis, J.A., Kent, D.B., 1990. Surface complexation modeling in aqueous geochemistry. Rev. Mineral. Geochem. 23 (1), 177e260.

Ding, S., Chen, P., Liu, S., Zhang, G., Zhang, J., Dan, S.F., 2019. Nutrient dynamics in the Changjiang and retention effect in the Three Gorges Reservoir. J. Hydrol. 574, 96–109. https://doi.org/10.1016/j.jhydrol.2019.04.034.

Dittmann, S., Baring, R., Baggalley, S., Cantin, A., Earl, J., Gannon, R., et al., 2015. Drought and flood effects on macrobenthic communities in the estuary of Australia's largest river system. Estuarine, Coast. Shelf Sci. 165 (C), 36–51. https://doi.org/10.1016/j.ecss.2015.08. 023.

Dore, J.E., Houlihan, T., Hebel, D.V., Tien, G., Tupas, L., Karl, D.M., 1996. Freezing as a method of sample preservation for the analysis of dissolved inorganic nutrients in

seawater. Mar. Chem. 53, 173–185. https://doi.org/10.1016/0304- 4203(96)00004-7.
Egbert, G.D., Erofeeva, S.Y., 2002. Efficient inverse modeling of barotropic ocean tides. J. Atmos. Oceanic Technol. 19 (2), 183–204.
Fennel, K., Testa, J.M., 2019. Biogeochemical Controls on Coastal Hypoxia. Annu. Rev. Mar. Sci. 11 (1), 105–130. https://doi.org/10.1146/annurev-marine-010318-095138.
Feng, L., Hu, C., Chen, X., Song, Q., 2014. Influence of the Three Gorges Dam on total suspended matters in the Yangtze Estuary and its adjacent coastal waters: Observations from MODIS. Remote Sens. Environ. 140 (C), 779–788. https://doi.org/10.1016/j.rse.2013. 10.002.
Froelich, P.N., 1988. Kinetic control of dissolved phosphorus in natural rivers and estuaries-a primer on the phosphate buffer mechanism. Limnol. Oceanogr. 33 (4), 649–668.
Gao, X., Fujiwara, M., Winemiller, K.Q., Lin, P., Li, M., Liu, H., 2019. Regime shift in fish assemblage structure in the Yangtze River following construction of the Three Gorges Dam. Sci. Rep. 9 (1), 1–11. https://doi.org/10.1038/s41598-019-38993-x.
Gao, L., Li, D., Ishizaka, J., Zhang, Y., Zong, H., Guo, L., 2015. Nutrient dynamics across the river-sea interface in the Changjiang (Yangtze River) estuary-East China Sea region. Limnol. Oceanogr. 60 (6), 2207–2221. https://doi.org/10.1002/lno.10196.
Gao, L., Li, D., Zhang, Y., 2012. Nutrients and particulate organic matter discharged by the Changjiang (Yangtze River): Seasonal variations and temporal trends. J. Geophys. Res.: Biogeosci., 117 (G). https://doi.org/10.1029/2012JG00 1952.
Ge, J., Torres, R., Chen, C., Liu, J., Xu, Y., Bellerby, R., Shen, F., Bruggeman, J., Ding, P., 2020a. Influence of suspended sediment front on nutrients and phytoplankton dynamics off the Changjiang Estuary: a FVCOM-ERSEM coupled model experiment. J. Mar. Syst. 204, 103292. https://doi.org/10.1016/j.jmarsys.2019.103292.
Ge, J., Shi, S., Liu, J., Xu, Y., Chen, C., Bellerby, R., Ding, P., 2020b. Interannual variabilities of nutrients and phytoplankton off the Changjiang Estuary in response to changing river inputs. J. Geophys. Res.: Oceans 125. https://doi.org/10.1029/2019JC015595 e2019JC015595.
Gierach, M.M., Vazquez-Cuervo, J., Lee, T., Tsontos, V.M., 2013. Aquarius and SMOS detect effects of an extreme Mississippi River flooding event in the Gulf of Mexico. Geophys. Res. Lett. 40 (19), 5188–5193. https://doi.org/10.1002/grl.v40.1910.1002/grl.50995.
Gong, G.-C., Liu, K.-K., Chiang, K.-P., Hsiung, T.-M., Chang, J., Chen, C.-C., Hung, C.-C., Chou, W.-C., Chung, C.-C., Chen, H.-Y., Shiah, F.-K., Tsai, A.-Y., Hsieh, C.-hao., Shiao, J.-C., Tseng, C.-M., Hsu, S.-C., Lee, H.-J., Lee, M.-A., Lin, I.-I., Tsai, F., 2011. Yangtze River floods enhance coastal ocean phytoplankton biomass and potential fish production. L13603 Geophys. Res. Lett. 38 (13). https://doi.org/10.1029/2011GL047519.
Gopal, V., Krishnakumar, S., Peter, T.S., Nethaji, S., Kumar, K.S., Jayaprakash, M., Magesh, N.S., 2017. Assessment of trace element accumulation in surface sediments off Chennai coast after a major flood event. Mar. Pollut. Bull. 114 (2), 1063–1071. https://doi.org/10.1016/j.marpolbul.2016.10.019.
Houghton, R., Tilburg, C., Garvine, R., Fong, A., 2004. Delaware River plume response to a strong upwelling-favorable wind event. Geophys. Res. Lett. 31 (7). L07302.
Howley, C., Devlin, M., Burford, M., 2018. Assessment of water quality from the Normanby River catchment to coastal flood plumes on the northern Great Barrier Reef, Australia. Mar. Freshwater Res. 69 (6), 859–915. https://doi.org/10.1071/MF17009.
Huang, L., Li, X., Fang, H., Yin, D., Si, Y., Wei, J., et al., 2019. Balancing social, economic, and ecological benefits of reservoir operation during the flood season: a case study of the Three Gorges Project, China. J. Hydrol. 572, 422–434. https://doi.org/10.1016/j.jhydrol. 2019.03.009.
Huret, M., Runge, J.A., Chen, C., Cowles, G., Xu, Q., Pringle, J.M., 2007. Dispersal modeling of early life stages: sensitivity analysis with application to Atlantic cod in the western Gulf of Maine. Mar. Ecol. Prog. Ser. 347, 261–274. https://doi.org/10.3354/meps06983.
Jiao, N., Zhang, Y., Zeng, Y., Gardner, W.D., Mishonov, A.V., Richardson, M.J., et al., 2007. Biogeochemical anomalies in the East China Sea: impacts of the Three Gorges Dam? Water Res. 41 (6), 1287–1293. https://doi.org/10.1016/j.watres.2006.11.053.
Jolliff, J.K., Kindle, J.C., Shulman, I., Penta, B., Friedrichs, M.A.M., Helber, R., Arnone, R.A., 2009. Summary diagrams for coupled hydrodynamic-ecosystem model skill assessment. J. Mar. Syst. 76 (1–2), 64–82. https://doi.org/10.1016/j.jmarsys.2008.05.014.
Kerimoglu, O., Voynova, Y.G., Chegini, F., Brix, H., Callies, U., Hofmeister, R., et al., 2020. Interactive impacts of meteorological and hydrological conditions on the physical and biogeochemical structure of a coastal system. Biogeosciences 17 (20), 5097–5127. https://doi.org/10.5194/bg-17-5097-2020.
Lou, X., Hu, C., 2013. Diurnal changes of a harmful algal bloom in the East China Sea: observations from GOCI. Remote Sens. Environ. 140, 1–11. https://doi.org/10.1016/j.rse.2013.09.031.
Luan, H.L., Ding, P.X., Wang, Z.B., Ge, J.Z., Yang, S.L., 2016. Decadal morphological evolution of the Yangtze Estuary in response to river input changes and estuarine engineering projects. Geomorphology 265, 12–23. https://doi.org/10.1016/j.geomorph.2016.04.022.
Mallin, M.A., Posey, M.H., McIver, M.R., Parsons, D.C., Ensign, S.H., Alphin, T.D., 2002. Impacts and recovery from multiple hurricanes in a Piedmont-coastal plain river system. Bioscience 52 (11), 999–1010. https://doi.org/10.1641/0006-3568(2002)052[0999:IARFMH] 2.0.CO;2.
Milliman, J.D., Farnsworth, K.L., 2011. River Discharge to the Coastal Ocean: A Global Synthesis. Cambridge University Press, Cambridge.
O'Mara, K., Olley, J.M., Fry, B., Burford, M., 2019. Catchment soils supply ammonium to the coastal zone – flood impacts on nutrient flux in estuaries. Sci. Total Environ. 654 (C), 583–592. https://doi.org/10.1016/j.scitotenv.2018.11.077.
Paerl, H.W., Pinckney, J.L., Fear, J.M., Peierls, B.L., 1998. Ecosystem responses to internal and watershed organic matter loading: consequences for hypoxia in the eutrophying Neuse River estuary, North Carolina, USA. Mar. Ecol. Prog. Ser. 16, 17–25.
Pan, G., Krom, M.D., Zhang, M., Zhang, X., Wang, L., Dai, L., et al., 2013. Impact of Suspended Inorganic Particles on Phosphorus Cycling in the Yellow River (China). Environ. Sci. Technol. 47 (17), 9685–9692. https://doi.org/10.1021/es4005619.
Reid, P.C., Colebrook, J.M., Matthews, J.B.L., Aiken, J., Barnard, R., Batten, S.D., et al., 2003. The Continuous Plankton Recorder: Concepts and history, from Plankton Indicator to undulating recorders. In: Presented at the Progress in Oceanography, pp. 117–173. https://doi.org/10.1016/j.pocean.2003.08.002.
Roy, E.D., White, J.R., Smith, E.A., Bargu, S., Li, C., 2013. Estuarine ecosystem response to three large-scale Mississippi River flood diversion events. Sci. Total Environ. 458–460, 374–387. https://doi.org/10.1016/j.scitotenv.2013.04.046.
Shi, W., Wang, M., 2009. Satellite observations of flood-driven Mississippi River plume in the spring of 2008. Geophys. Res. Lett. 36 (7), L07607. https://doi.org/10.1029/2009GL037210.
Shulkin, V., Tishchenko, P., Semkin, P., Shvetsova, M., 2018. Influence of river discharge and phytoplankton on the distribution of nutrients and trace metals in Razdolnaya River estuary, Russia, Estuar. Coast. Shelf Sci. 1–11 https://doi.org/10.1016/j.ecss.2017. 09.024.
Talbot, C.J., Bennett, E.M., Cassell, K., Hanes, D.M., Minor, E.C., Paerl, H., Raymond, P. A., Vargas, R., Vidon, P.G., Wollheim, W., Xenopoulos, M.A., 2018. The impact of flooding on aquatic ecosystem services. Biogeochemistry 141 (3), 439–461. https://doi.org/10.1007/s10533-018-0449-7.
Taylor, K.E., 2001. Summarizing multiple aspects of model performance in a single diagram. J. Geophys. Res. Atmos. 106 (D7), 7183–7192. https://doi.org/10.1029/2000JD900719.
Tian, R., 2019. Factors controlling saltwater intrusion across multi-time scales in estuaries, Chester River, Chesapeake Bay, Estuarine. Coast. Shelf Sci. 223, 61–73. https://doi.org/10.1016/j.ecss.2019.04.041.
Tullos, D., 2009. Assessing the influence of environmental impact assessments on science and policy: an analysis of the Three Gorges Project. J. Environ. Manage. 90, S208–S223. https://doi.org/10.1016/j.jenvman.2008.07.031.
Tyler, K.J., Becker, A., Moltschaniwskyj, N.A., Taylo, M.D., 2017. Rapid salinity changes affect the survival and physiology of a penaeid prawn: Implications of flood events on recruitment to the fishery. Fish. Manage. Ecol. 24 (6), 478–487. https://doi.org/10.1111/fme.12256.
Voynova, Y.G., Brix, H., Petersen, W., Weigelt-Krenz, S., Scharfe, M., 2017. Extreme flood impact on estuarine and coastal biogeochemistry: the 2013 Elbe flood. Biogeosciences 14 (3), 541–557. https://doi.org/10.5194/bg-14-541-2017.
Wetz, M.S., Yoskowitz, D.W., 2013. An "extreme" future for estuaries? Effects of extreme climatic events on estuarine water quality and ecology. Mar. Pollut. Bull. 69 (1-2), 7–18. https://doi.org/10.1016/j.marpolbul.2013.01.020.
Xinhua News Agency, 2010. China's Three Gorges Dam project stands biggest flood-control test. <http://news.xinhuanet.com/english2010/photo/2010-07/20/c_13406457.htm> (July, 20, 2010).
Xinhua News Agency, 2012. Three Gorges Dam withstands huge flood. <http://news.xinhuanet.com/english/video/2012-07/25/c_131737567.htm> (July,25,2012).
Xu, X., Tan, Y., Yang, G., 2013. Environmental impact assessments of the Three Gorges Project in China: Issues and interventions. Earth-Sci. Rev. 124 (C), 115–125. https://doi.org/10.1016/j.earscirev.2013.05.007.
Yankovsky, A.E., Chapman, D.C., 1997. A simple theory for the fate of Buoyant coastal discharges. J. Phys. Oceanogr. 27 (7), 1386–1401.
Yang, S.L., Milliman, J.D., Li, P., Xu, K., 2011. 50,000 dams later: Erosion of the Yangtze River and its delta. Global Planet. Change 75 (1–2), 14–20. https://doi.org/10.1016/j.gloplacha.2010.09.006.
Yang, S.L., Xu, K.H., Milliman, J.D., Yang, H.F., Wu, C.S., 2015. Decline of Yangtze River water and sediment discharge: Impact from natural and anthropogenic changes. Sci. Rep. 1–14 https://doi.org/10.1038/srep12581.
Yu, D., Chen, N., Krom, M.D., Lin, J., Cheng, P., Yu, F., Guo, W., Hong, H., Gao, X., 2019. Understanding how estuarine hydrology controls ammonium and other inorganic nitrogen concentrations and fluxes through the subtropical Jiulong River Estuary, S. E. China under baseflow and flood-affected conditions. Biogeochemistry 142 (3), 443–466. https://doi.org/10.1007/s10533-019-00546-9.
Zhang, J.-Z., Ortner, P.B., 1998. Effect of thawing condition on the recovery of reactive silicic acid from frozen natural water samples. Water Res. 32 (8), 2553–2555. https://doi.org/10.1016/S0043-1354(98)00005-0.
Zhang, X., Dong, Z., Gupta, H., Wu, G., Li, D., 2016. Impact of the Three Gorges Dam on the hydrology and ecology of the Yangtze River. Water 8 (12). https://doi.org/10.3390/w8120590, 590–18.
Zhang, J., Chen, L., 2017. Regulation effects of Three Gorges Reservoir and flood forecast for No. 1 flood in 2016 of Changjiang River, Yangtze River, 48(04):13-15+36. http://doi.org/10.16232/j.cnki.1001-4179.2017.04.013 (In Chinese with English abstract).
Zheng, S., 2017. Regulation effects and flood defense of Three Gorges Reservoir: taking flood events in 2016 as examples. Technol. Econo. Changjiang 1, 38–42 (in Chinese).
Zhu, Z.-Y., Zhang, J., Wu, Y., Zhang, Y.-Y., Lin, J., Liu, S.-M., 2011. Hypoxia off the Changjiang (Yangtze River) Estuary: Oxygen depletion and organic matter

decomposition. Mar. Chem. 125 (1-4), 108–116. https://doi.org/10.1016/j.marchem.2011.03.005.
Zhu, Z.Y., Ng, W.M., Liu, S.M., Zhang, J., Chen, J.C., Wu, Y., 2009. Estuarine phytoplankton dynamics and shift of limiting factors: a study in the Changjiang (Yangtze River) Estuary and adjacent area. Estuar. Coast. Shelf Sci. 84 (3), 393–401. https://doi.org/10.1016/j.ecss.2009.07.005.
Zoppini, A., Ademollo, N., Bensi, M., Berto, D., Bongiorni, L., Campanelli, A., Casentini, B., Patrolecco, L., Amalfitano, S., 2019. Impact of a river flood on marine water quality and planktonic microbial communities, Estuar. Coast. Shelf Sci. 224, 62–72. https://doi.org/10.1016/j.ecss.2019.04.038.